



HST Imaging of Star-forming Clumps in Six GASP Ram-pressure-stripped Galaxies

Eric Giunchi^{1,2} , Marco Gullieuszik¹ , Bianca M. Poggianti¹ , Alessia Moretti¹ , Ariel Werle¹ , Claudia Scarlata³ ,
Anita Zanella¹ , Benedetta Vulcani¹ , and Daniela Calzetti⁴

¹ INAF-Osservatorio astronomico di Padova, Vicolo Osservatorio 5, I-35122 Padova, Italy

² Dipartimento di Fisica e Astronomia, Università di Padova, Vicolo Osservatorio 3, I-35122 Padova, Italy

³ Minnesota Institute for Astrophysics, School of Physics and Astronomy, University of Minnesota, 316 Church Street SE, Minneapolis, MN 55455, USA

⁴ Department of Astronomy, University of Massachusetts, 710 North Pleasant Street, LGRT 619J, Amherst, MA 01002, USA

Received 2022 November 23; revised 2023 February 20; accepted 2023 March 3; published 2023 June 6

Abstract

Exploiting broad- and narrowband images of the Hubble Space Telescope from the near-UV to *I*-band rest frame, we study the star-forming clumps of six galaxies of the GASP sample undergoing strong ram pressure stripping. Clumps are detected in $H\alpha$ and near-UV, tracing star formation on different timescales. We consider clumps located in galaxy disks and stripped tails and formed in stripped gas but still close to the disk, called extraplanar. We detect 2406 $H\alpha$ -selected clumps (1708 in disks, 375 in extraplanar regions, and 323 in tails) and 3745 UV-selected clumps (2021 disk, 825 extraplanar, and 899 tail clumps). Only $\sim 15\%$ of star-forming clumps are spatially resolved, meaning that most are smaller than ~ 140 pc. We study the luminosity and size distribution functions (LDFs and SDFs, respectively) and the luminosity–size relation. The average LDF slope is 1.79 ± 0.09 , while the average SDF slope is 3.1 ± 0.5 . The results suggest that the star formation is turbulence-driven and scale-free, as in main-sequence galaxies. All of the clumps, whether they are in the disks or tails, have an enhanced $H\alpha$ luminosity at a given size, compared to the clumps in main-sequence galaxies. Indeed, their $H\alpha$ luminosity is closer to that of clumps in starburst galaxies, indicating that ram pressure is able to enhance the luminosity. No striking differences are found among disk and tail clumps, suggesting that the different environments in which they are embedded play a minor role in influencing the star formation.

Unified Astronomy Thesaurus concepts: [Galaxy clusters \(584\)](#); [Galaxy evolution \(594\)](#); [Star formation \(1569\)](#); [Star forming regions \(1565\)](#); [Galaxy structure \(622\)](#); [Galaxy tails \(2125\)](#)

Supporting material: figure set, machine-readable table

1. Introduction

Star formation is the mechanism driving the condensation of atomic gas from galactic to subkiloparsec scales down to the dense cores (on parsec/subparsec scales) in which stars eventually form (Section 4 of Kennicutt & Evans 2012); therefore, studying which processes are capable of influencing it is fundamental to our understanding of galaxy formation and evolution. The bridge between the galactic- and core-scale regimes is represented by $\gtrsim 10$ pc-scaled star-forming clumps with masses $\gtrsim 10^4 M_\odot$ (Portegies Zwart et al. 2010). Our knowledge about these structures has greatly improved in the last decade thanks to observational surveys of low-redshift galaxies with the Hubble Space Telescope (HST), which is able to achieve the resolution necessary to study their morphology and size properties (LEGUS, Calzetti et al. 2015; DYNAMO, Fisher et al. 2017; LARS, Messa et al. 2019; PHANGS-HST; Lee et al. 2020). Exploiting LEGUS data, many studies find hints that star formation is a turbulence-driven process fragmenting the gas following a scale-free hierarchy (Elmegreen et al. 2014; Gouliermis et al. 2015, 2017). The hierarchical structure is then also reflected in the emerging spatial distribution of stars formed from such gas (Elmegreen & Falgarone 1996; Elmegreen 2006; Grasha et al. 2017).

Moreover, the star formation mechanism can be strongly influenced by the properties of the local medium in which the

star-forming clumps form, and this leaves an imprint that can be studied using different diagnostics.

Models describing the fragmentation of star-forming regions as a scale-free, turbulence-driven process predict the mass distribution function of these regions to be a power law with slope 2 (Elmegreen 2006). The corresponding luminosity distribution function (LDF), if derived using a tracer of a narrow age range, is expected to have a similar slope, provided that (1) the initial mass function (IMF) is well sampled and independent of the mass of the initial cloud from which the clumps are formed and (2) the star formation history and therefore the stellar age distributions of all clouds are the same (Elmegreen & Falgarone 1996; Elmegreen 2006).

Indeed, from the observational point of view, the LDFs of recently formed star-forming regions are known to be well described by a power law, independent of wavelength, with a drop at luminosities fainter than a peak luminosity L_{peak} due to incompleteness (e.g., $H\alpha$, Kennicutt et al. 1989; Santoro et al. 2022; UV Cook et al. 2016; Messa et al. 2019; *V* band, Larsen 2002; Bastian et al. 2007; *R* band, Whitmore et al. 2014; IR and radio, Mascoop et al. 2021). In general, the observed slopes are found to be consistent with 2, even though in some cases there are hints of a slope slightly smaller than 2 (1.76 ± 0.3 , Cook et al. 2016; 1.73 ± 0.15 , Santoro et al. 2022). Interestingly, some of these works find the value of the slope to be affected by the local environment. Cook et al. (2016) and Santoro et al. (2022) showed that the LDF flattens in regions with a high star formation rate (SFR) surface density (Σ_{SFR}). The same trend is then reflected in the LDF of clumps belonging to different intergalactic environments; Messa et al. (2018) showed that the LDF of UV



Original content from this work may be used under the terms of the [Creative Commons Attribution 4.0 licence](#). Any further distribution of this work must maintain attribution to the author(s) and the title of the work, journal citation and DOI.

clumps in the spiral arms of the LEGUS galaxy M51 is flatter than that of clumps in the interarm region (with likely lower Σ_{SFR}).

The size distribution function (SDF) of the star-forming clumps is known to be well described by a power law as well (Kennicutt & Hodge 1980; Gusev 2014), with slopes between 2.5 and 4.5 and a flatter distribution for an increasing level of clustering in the clumps.

The luminosity (typically $L_{\text{H}\alpha}$)–size relation, which many works (Wisnioski et al. 2012; Cosens et al. 2018 and references therein) have shown to be a linear relation in the logarithmic plane, is another proxy of the properties of star formation. The slope and the normalization of the correlation are thought to be related to the geometrical properties of the H II regions ionized by young stars and to the SFR surface density Σ_{SFR} . As shown in Cosens et al. (2018), clumps in starburst-like environments, and therefore with a high Σ_{SFR} , are likely to have a higher $\text{H}\alpha$ luminosity at a given size and follow a flatter distribution.

Jellyfish galaxies are a great laboratory to study star formation in peculiar regimes and environments. Jellyfish galaxies are cluster galaxies undergoing strong ram pressure stripping (RPS; Gunn et al. 1972). The ram pressure exerted by the intracluster medium (ICM) is able to strip the gas from the galactic interstellar medium (ISM), eventually producing tails up to more than 100 kpc long but leaving the stellar disk almost undisturbed (Poggianti et al. 2017a). The gas removal accelerates the quenching of the star formation in the galaxy (Cortese et al. 2021). Several previous works find RPS to be able to briefly enhance star formation during the first stages of the stripping process and trigger in situ star formation in compact knots of gas stripped out of the galactic disks (Yoshida et al. 2008; Smith et al. 2010; Merluzzi et al. 2013; Fossati et al. 2016; Consolandi et al. 2017; Jáchym et al. 2019). The tails of these galaxies give the unprecedented opportunity to study the star formation mechanism in a hotter and higher-pressure environment than the galactic ISM and without the influence of the underlying contamination of the old stellar populations in the disk.

Abramson & Kenney (2014) and Kenney et al. (2015) observed galaxies undergoing RPS in the Virgo (NGC 4402 and NGC 4522) and Coma (NGC 4921) clusters, respectively, with HST. These works show that RPS is able to decouple the high-density component of the ISM (in particular, the giant molecular clouds) from the low-density one, which is more prone to stripping. Also, dust is characterized by elongated morphology and filaments aligned with the stripping direction. Cramer et al. (2019) studied the long and narrow $\text{H}\alpha$ tail of D100 in the Coma cluster with HST and found unbound young UV sources with sizes of $\sim 50\text{--}100$ pc, which they considered likely to disperse with aging.

One of the aims of the GAs Stripping Phenomena in galaxies with MUSE (GASP; Poggianti et al. 2017a) ESO Large Program is to study the properties of galaxies affected by different gas removal processes in the field, groups, and clusters. This includes cluster galaxies in different RPS stages from pre- (the control sample) to poststripping (Fritz et al. 2017). Targets were chosen from the catalog in Poggianti et al. (2016) as galaxies with long unilateral debris in optical images, suggestive of gas-only removal. The final sample includes galaxies in the mass range $10^9\text{--}10^{11.5} M_{\odot}$ and at redshift $0.04 < z < 0.07$. Targets were observed with the Multi Unit Spectroscopic Explorer (MUSE) on the Very Large Telescope (details about the MUSE data are given in Section 2.2) in order to investigate the properties of both the ionized gas phase and

the stellar component in the disks and stripped tails. The results of GASP confirmed the presence of clumps with in situ star formation in the tails of individual jellyfish galaxies of the sample (Bellhouse et al. 2017; Gullieuszik et al. 2017; Moretti et al. 2018; Poggianti et al. 2019; Moretti et al. 2020). In particular, Poggianti et al. (2019) analyzed star-forming clumps in the tails and disks of 16 GASP galaxies, finding that the tail clumps are less massive in terms of both stellar and gas mass and have a smaller gas velocity dispersion than the clumps in the disks. However, the spatial resolution of MUSE at the typical redshift of the GASP galaxies (~ 1 kpc) did not allow us to study the morphology and size of these clumps.

In order to better characterize the properties of the star-forming clumps detected in GASP galaxies with MUSE, six galaxies of the GASP sample have been observed with HST, whose resolution is about a factor of 14 better than that of MUSE (details in Section 2.1). The broadband filters that were adopted are F275W, F336W, F606W, and F814W, covering a spectral range going from the UV to *I*-band rest frame. In addition, galaxies were also observed with the narrowband filter F680N, collecting the $\text{H}\alpha$ emission.

This paper is structured as follows. In Section 2, we present the HST and MUSE data; in Section 3, we define the spatial categories; Section 4 is focused on the steps followed for detecting and selecting star-forming clumps and complexes; in Section 5, we present the samples of clumps and complexes; in Section 6, we study the LDFs and SDFs of clumps and complexes (Sections 6.1 and 6.2, respectively); Section 7 is dedicated to the luminosity–size relation of the clumps; in Section 8, the catalogs that will be publicly available are described; and in Section 9, we summarize our results.

This paper adopts the standard concordance cosmology parameters $H_0 = 70 \text{ km s}^{-1} \text{ Mpc}^{-1}$, $\Omega_M = 0.3$, and $\Omega_{\Lambda} = 0.7$ and a Chabrier (2003) IMF.

2. Data

2.1. HST Data

In this work, we focus on the study of the luminosities and sizes of the star-forming clumps and complexes in a subsample of six GASP galaxies whose main properties are listed in Table 1. The galaxies were selected from the GASP sample of ram-pressure-stripped galaxies (Poggianti et al. 2017b) for their extended $\text{H}\alpha$ -emitting tails and, in particular, the large number of $\text{H}\alpha$ clumps detected with MUSE observations (Poggianti et al. 2019; see also Vulcani et al. 2020).

The galaxies were observed using the WFC3/UVIS on board HST using four broadband filters (F275W, F336W, F606W, and F814W) that cover a spectral range from the UV to *I*-band rest frame. In addition, galaxies were also observed with a narrowband filter, F680N, in order to collect the $\text{H}\alpha$ emission at the redshift of these galaxies. Details of the observations, data reduction, calibration and analysis, estimate of the standard deviation of the background in each band (σ), and $\text{H}\alpha + [\text{N II}]$ extraction from the F680N band are described in Gullieuszik et al. (2023), but here we summarize the most important properties.

All images collected have a pixel angular size of $0''.04$. The UVIS point-spread functions (PSFs) in all five filters do not change significantly and have an FWHM of $0''.07$,⁵

⁵ <https://hst-docs.stsci.edu/wfc3ihb/chapter-6-uvis-imageing-with-wfc3/6-6-uvis-optical-performance>

Table 1
Summary of the Main Properties of the Galaxies Studied in This Paper and Their Host Clusters

ID _{P16}	R.A. (J2000)	Decl. (J2000)	M_* $10^{10} M_\odot$	$\frac{H\alpha}{H\alpha + [N II]}$	z_{gal}	Cluster	σ_{clus} $km s^{-1}$	z_{clus}	References
(1)	(2)	(3)	(4)	(5)	(6)	(7)	(8)	(9)	(10)
JO175	20:51:17.593	-52:49:22.34	$3.2_{2.7}^{3.7}$	0.705	0.0468	A3716	753_{-38}^{+36}	0.0457	4, 10, 14
JO201	00:41:30.295	-09:15:45.98	$6.2_{2.4}^{7.0}$	0.660	0.0446	A85	859_{-44}^{+42}	0.0559	3, 4, 5, 6, 8, 9, 10, 13, 14, 15, 16, 18
JO204	10:13:46.842	-00:54:51.27	$4.1_{13.5}^{4.7}$	0.660	0.0424	A957	631_{-40}^{+43}	0.0451	2, 4, 6, 12, 18
JO206	21:13:47.410	+02:28:35.50	$9.1_{8.2}^{10.0}$	0.703	0.0513	IIZW108	575_{-31}^{+33}	0.0486	1, 4, 6, 10, 13, 18, 19
JW39	13:04:07.719	+19:12:38.41	17_{14}^{20}	0.650	0.0650	A1668	654	0.0634	14, 18, 19, 21
JW100	23:36:25.054	+21:09:02.64	29_{22}^{36}	0.530	0.0602	A2626	650_{-49}^{+53}	0.0548	4, 6, 7, 10, 11, 15, 17, 18, 19, 20

Note. Columns are (1) GASP ID of the galaxy as in Poggianti et al. (2016), (2) and (3) R.A. and decl. of the galaxy, (4) galaxy stellar mass, (5) median value for $H\alpha$ / ($H\alpha + [N II]$) from the MUSE clumps listed in Poggianti et al. (2019), (6) galaxy redshift, (7) ID of the host cluster, (8) cluster velocity dispersion, (9) cluster redshift, and (10) references. References are (1) Poggianti et al. (2017a), (2) Gullieuszik et al. (2017), (3) Bellhouse et al. (2017), (4) Poggianti et al. (2017b), (5) George et al. (2018), (6) Moretti et al. (2018), (7) Poggianti et al. (2019), (8) Bellhouse et al. (2019), (9) George et al. (2019), (10) Radovich et al. (2019), (11) Moretti et al. (2020), (12) Deb et al. (2020), (13) Ramatsoku et al. (2020), (14) Bellhouse et al. (2021), (15) Tomičić et al. (2021a), (16) Campitiello et al. (2021), (17) Ignesti et al. (2022a), (18) Tomičić et al. (2021b), (19) Ignesti et al. (2022b), (20) Sun et al. (2021), and (21) Peluso et al. (2022). Masses are taken from Vulcani et al. (2018). Cluster redshifts and velocity dispersions are taken from Cava et al. (2009) and Biviano et al. (2017).

corresponding to ~ 70 pc at the redshifts of the clusters hosting these galaxies (0.0424–0.0650; see Table 1). Images were reduced and calibrated using ASTRODRIZZLE.⁶ To obtain the $H\alpha + [N II]$ maps, the continuum emission is modeled by linearly interpolating the emission coming from broadband filters F606W and F814W and then subtracted from the F680N images. Contamination from emission lines within the two broadband filters is expected to have only a small ($< 10\%$) impact on our $H\alpha$ intensity estimates (see Gullieuszik et al. 2023).

For our purposes, in some cases, we are also going to work with denoised versions of these HST images. Denoising is performed using a Python software package called PYSAP⁷ (Farrens et al. 2020). This algorithm expands the image in Fourier series, and we set its parameters in order to remove the high-frequency components, which are typically due to noise. We removed the component with the highest frequency, equal to 2 pixels. This procedure allows us to also detect fainter regions without being dominated by noise but does not yield reliable sizes. This is the reason for not working with denoised images alone.

Throughout this paper, we work on a smaller squared field of view (FOV; see Table 2) with respect all of the HST-WFC3/UVIS images ($2' 67 \times 2' 67$), still sufficient to cover the entire extension of the galaxies and their tails.

2.2. MUSE Data

Throughout this work, we also exploit the information obtained from the GASP survey to remove regions powered by active galactic nuclei (AGN) or shocks using BPT maps (Baldwin et al. 1981), confirm the redshift of star-forming clump candidates, and correct the F680N filter for the line emission of N II. All galaxies were observed in service mode with MUSE (Bacon et al. 2010). MUSE is an integral field unit spectrograph with a $1' \times 1'$ FOV sampled with $0''.2 \times 0''.2$ pixels. The typical seeing of the MUSE observations is $1''$ (0.7–1.3 kpc at the redshifts of these galaxies; Table 1).

⁶ <https://drizzlepac.readthedocs.io/en/latest/CHANGELOG.html>

⁷ <https://cea-cosmic.github.io/pysap/index.html>

Table 2
Properties of the HST Images Sub-FOV Used to Detect Clumps

ID _{P16}	R.A. _{center}	Decl. _{center}	Width
JO175	20:51:17.6169	-52:49:47.189	2'00
JO201	0:41:31.7471	-9:16:02.613	2'67
JO204	10:13:47.2256	-0:54:46.617	1'60
JO206	21:13:44.1417	+2:28:06.535	3'27
JW39	13:04:08.8132	+19:12:17.151	2'20
JW100	23:36:23.0832	+21:04:47.508	1'93

Note. For each galaxy (ID_{P16}), the center coordinates (R.A._{center} and decl._{center}) and the width of the sub-FOV (width) are listed. The sub-FOV are always squared.

Furthermore, MUSE spectra cover a spectral range from 4500 to 9300 Å sampled at $\sim 1.25 \text{ \AA pixel}^{-1}$ and with a spectral resolution of 2.6 Å. The data were reduced using the most recent version of the MUSE pipeline available at the time of each observation (Bacon et al. 2010; from version 1.2 to 1.6), as described in detail in Poggianti et al. (2017a). The data cubes were then corrected for Galactic extinction using the extinction law and the reddening map by Cardelli et al. (1989) and Schlegel et al. (1998; considering the recalibration introduced by Schlafly & Finkbeiner 2011), respectively. The fluxes, velocities, and velocity dispersions of the gas emission lines were obtained using KUBEVIZ (Fossati et al. 2016) after subtracting the stellar-only component derived with SINOPSIS (Fritz et al. 2017).

3. Definition of Disk, Extraplanar, and Tail Regions

Throughout this work, we are interested in studying the effects of the local environment on star formation; thus, we aim at distinguishing star-forming regions originating from stripped gas embedded in the cluster environment from those still in the galaxy disk.

In analogy with what was done for the MUSE observations (Gullieuszik et al. 2020), the starting point to define the stripped tails is the definition of the galaxy stellar disk. As already noted in Gullieuszik et al. (2023; see also Figure 1), the high spatial resolution of HST allows us to characterize the

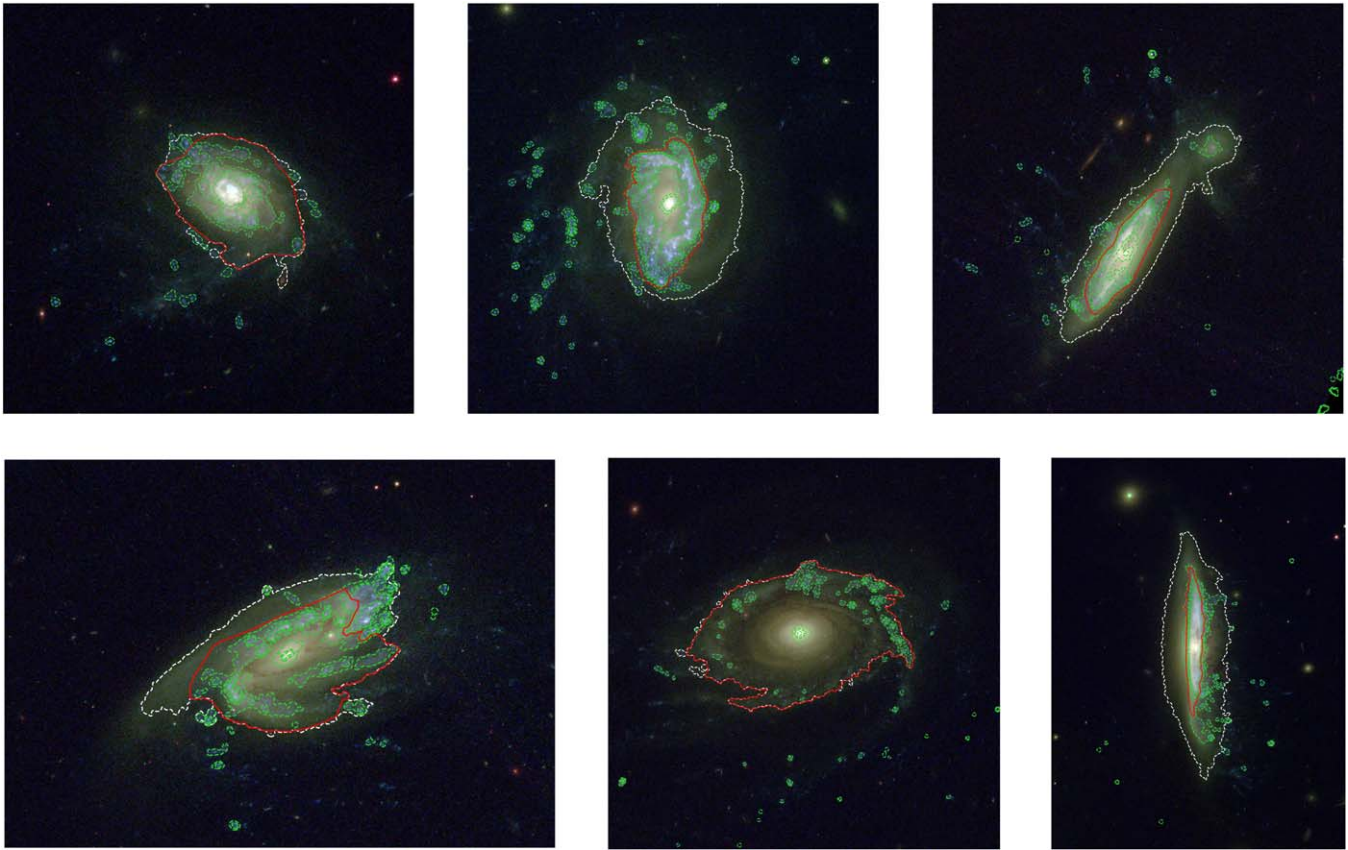


Figure 1. Zoomed-in RGB images of JO175, JO201, JO204, JO206, JW39, and JW100 (from top left to bottom right). The three colors of the RGB images are F814W (red), F606W (green), and a combination of F275W, F606W, and F814W (blue). Details are given in Gullieuszik et al. (2023). The white dashed contours are the optical disks, defined as the 2σ contour in F814W. The green dashed contours are the 1σ , 2σ , 3σ , and 5σ UV (F275W+F336W) contours (smoothed for clarity). The red solid line is the inner disk contour, traced as described in Section 3.

galaxy substructures and the stellar disk in more detail than what is possible with MUSE. We used the 2σ contour of the reddest photometric band available (F814W) to draw the most external boundary of the stellar optical disk. The 2σ values range from 2.14 to $2.67 \times 10^{-21} \text{ erg s}^{-1} \text{ cm}^{-2} \text{ \AA}^{-1} \text{ pixel}^{-1}$. We will refer to this contour as the galaxy optical contour (white dashed lines in Figure 1), and we define as the tail the region beyond it.

In the disks of these galaxies, there are some regions that are particularly bright in UV (band F275W), faint in optical (band F814W), elongated, and aligned in the same direction as the tails. Therefore, they are likely to be young stellar populations formed in gas already stripped by ram pressure but still inside the galaxy optical contour because of projection effects or because RPS is at an early stage; we call these regions extraplanar. In order to separate the extraplanar regions from those still in the disk, we visually inspected the RGB images and traced an inner disk contour (red solid lines in Figure 1) using the UV contours of the images as a guide (green dashed contours in Figure 1) to separate clumps that are elongated in appearance and aligned along the likely stripping direction from those that are not. We define as “disk” the region within the inner disk contour and as “extraplanar” the region within the galaxy optical contour but outside the inner disk contour. We point out that this process cannot completely separate undisturbed and stripped gas, since it is done via visual inspection, and projection effects may prevent a perfect separation of these two categories of gas.

4. Clump and Complex Detection

This section presents the procedure we developed to detect star-forming clumps and measure their properties. This procedure was applied independently to both the F275W and H α images (Section 4.2) in order to trace star formation on different timescales (~ 200 and ~ 10 Myr, respectively; Kennicutt 1998; Kennicutt & Evans 2012; Haydon et al. 2020). In addition, a different version of it is applied to the F606W images to fully recover the stellar content in the galaxy tails (Section 4.3).

4.1. Preliminary Steps and ASTRODENDRO Performance

As a first step, foreground and background sources are masked out. This is done using, when available, the spectroscopic information from MUSE and by visually inspecting the RGB images constructed as described in Gullieuszik et al. (2023), looking for red elliptical or blue spiral-armed sources, likely to be early-type and spiral galaxies, respectively.

The clump detection is performed using ASTRODENDRO,⁸ a software package created to compute dendrograms of observed or simulated astronomical data, classifying them in a hierarchical tree structure. With this software, we are able to detect not only bright clumps but also subclumps inside them. Figure 2 shows an illustration of three possible structures that ASTRODENDRO can generate.

⁸ <http://www.dendrograms.org/>

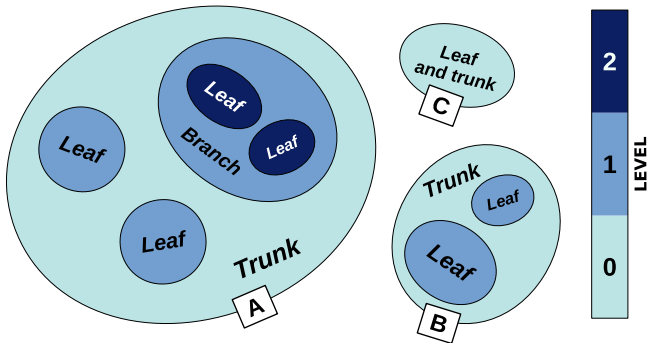


Figure 2. Illustration of the dendrogram structures built by ASTRODENDRO. Each clump is labeled with its position (trunk, branch, and leaf) and colored according to its level in the tree hierarchy (from zero to 2).

Clumps are defined as local maxima on the image; then the image is analyzed at fainter and fainter flux levels, and the clumps grow by including fainter pixels. Eventually, at some point, adjacent clumps might blend together. In this case, those clumps stop growing and are defined as children of a common parent clump; for the following steps, when fainter flux levels are considered, only the parent clump keeps growing. When the flux threshold reaches a given value (see `MIN_VALUE` in the [Appendix](#)), the algorithm stops and the tree structure is built, starting from the clumps at the base of the tree (i.e., the most extended ones), to which a level equal to zero is assigned. ASTRODENDRO retraces the tree and assigns to the subclumps a level equal to the level of their parent clump +1. It also generates a mask to define all pixels corresponding to each clump.

The naming convention used to define the position of the clump in the tree hierarchy is as follows:

1. *trunk*: clump with level = 0, regardless of whether it contains subclumps or not;
2. *branch*: clump with level > 0 and parent of other clumps; and
3. *leaf*: clump with no children subclumps. Notice that, according to this definition, a trunk can also be a leaf.

4.1.1. Observed Properties

For all of the detected clumps, the following quantities are computed by ASTRODENDRO:

1. the intensity-weighted mean position of the clump in the plane of the sky, hereafter adopted as clump center;
2. semimajor and semiminor axes computed as standard deviations of the flux distribution of the clump in the direction of greatest elongation in the plane of the sky;
3. the radius r_{core} computed as the geometric mean of the major and minor axes; and
4. the exact area of the clump on the plane of the sky A .

In addition, we computed the following quantities.

1. Flux densities for all of the photometric bands, integrated over the clump area A . The flux uncertainties are computed summing two contributions in quadrature: the background noise, computed as a function of the clump area as described in Gullieuszik et al. (2023), and the Poissonian uncertainty on the source counts converted

into flux considering the conversion factor PHOTFLAM, the exposure time, and the Milky Way dust attenuation.

2. Luminosity. This is calculated from the flux densities using the redshift of the cluster hosting the galaxy (column (8) in Table 1). In order to get $H\alpha$ luminosities, we compute $H\alpha/(H\alpha + [N II])$ for the $H\alpha$ clumps detected with MUSE in the galaxies of our sample (Poggianti et al. 2019). The median values obtained for each galaxy are listed in Table 1 and used to correct the F680N line flux for the $N II$ emission lines.
3. $r_{\text{core,corr}}$, the PSF-corrected core radius. It is computed by subtracting in quadrature the σ of the PSF ($\text{FWHM}/2\sqrt{35} \simeq 0''.03$; see Section 2.1) from r_{core} , and it is converted in physical scale according to the redshift of the hosting cluster of each galaxy.
4. Isophotal radius, defined as

$$r_{\text{iso}} = \sqrt{\frac{A}{\pi}}. \quad (1)$$

5. Size, defined as $2r_{\text{core,corr}}$. This choice is supported by the fact that $r_{\text{core,corr}}$ is defined by the flux distribution of the clump; therefore, it is less sensitive to the flux threshold above which clumps are detected (Wisnioski et al. 2012). Similar to Wisnioski et al. (2012), in Figure 3, we twice plot the PSF-corrected core radius against the isophotal radius to show that these two quantities almost follow a 1:1 relation.⁹

4.2. Star-forming Clumps

Star-forming clumps are identified in the F275W (UV-selected clumps) and $H\alpha$ ($H\alpha$ -selected clumps) images running ASTRODENDRO with a flux threshold of 2.5σ on the original images and 2σ on the denoised images.¹⁰ The two samples are computed independently, meaning that, in principle, some UV- and $H\alpha$ -selected clumps may overlap if the same region is bright enough in both filters. Details of the parameters set for ASTRODENDRO and the methods can be found in the [Appendix](#). Throughout the paper, we use only leaf and trunk clumps (LT sample), unless otherwise stated, to avoid considering the same region too many times.

ASTRODENDRO detected an initial total of 6090 $H\alpha$ and 6259 UV candidates. To minimize the number of spurious detections, we adopted the following procedure, which is schematized in the flowchart shown in Figure 4.

First, for each of the five photometric bands, we flagged a clump as detected if its flux has a signal-to-noise ratio (S/N)¹¹ higher than 2. We then exclude all clumps that were not detected in at least three photometric bands or in both F275W and F680N.¹² These criteria yield a reliable detection of clumps, as confirmed by subsequent visual inspection. A total of 3611 $H\alpha$ and 2293 UV spurious detections were removed. As an example, in Figure 5, we show the images in the five

⁹ In our size range, Wisnioski et al. (2012) also found that their isophotal radii are larger than the core radii by a factor of ~ 2 .

¹⁰ The 2σ threshold varies from galaxy to galaxy, ranging from 1.30 to $1.62 \times 10^{-20} \text{ erg s}^{-1} \text{ cm}^{-2} \text{ \AA}^{-1}$ for F275W and from 1.78 to $2.20 \times 10^{-18} \text{ erg s}^{-1} \text{ cm}^{-2}$ for $H\alpha$. More details on how these values are computed can be found in Gullieuszik et al. (2023).

¹¹ Defined as the ratio between the total flux of the clump and the noise of the image in an area as large as that of the clump.

¹² The reason for this is that a star-forming clump might, in principle, be bright in UV and $H\alpha$ only.

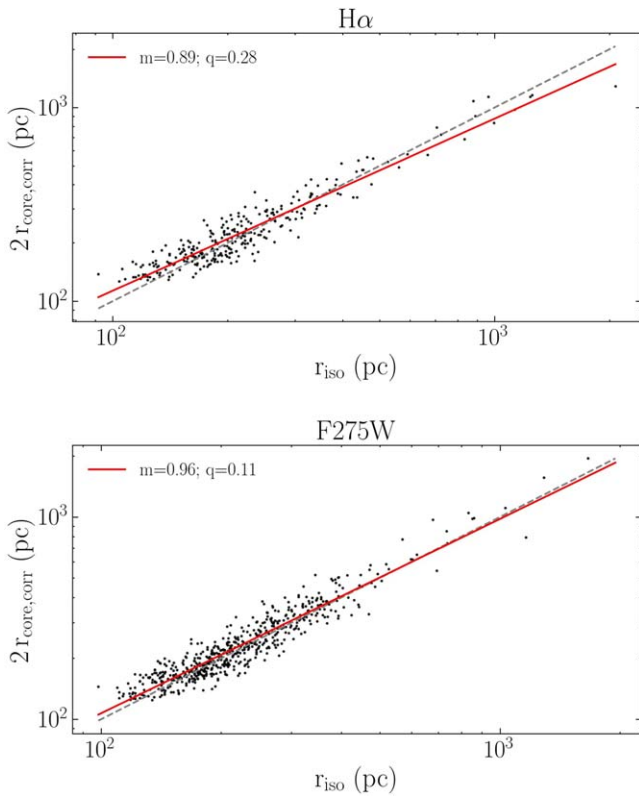


Figure 3. Comparison between the isophotal radius (r_{iso}) and twice the PSF-corrected core radius ($2r_{\text{core,corr}}$), defined in Section 4.1.1, for both $\text{H}\alpha$ - (top panel) and UV- (bottom panel) resolved clumps. The gray dashed line is the 1:1 relation, while the red solid line is the best-fitting line. The best-fitting line is in good agreement with the 1:1 relation for both $\text{H}\alpha$ - and UV-resolved clumps.

filters and $\text{H}\alpha$ of four $\text{H}\alpha$ -selected clump candidates of JO201. The first one (top left panels) is clearly detected in all images; the second one (top right panels) does not show UV emission but is detected in three optical filters and $\text{H}\alpha$; and the third one (bottom left panels) is detected only in F680N, F275W, and $\text{H}\alpha$. These three are therefore confirmed star-forming clumps. The last one (bottom right panels) shows emission only in F680N and $\text{H}\alpha$ and was therefore rejected.

Outside the stellar disk, ASTRODENDRO is more prone to detect residual cosmic rays and noise peaks as clump candidates in the tails. Cosmic rays and noise peaks are typically compact and bright, like the star-forming clumps we aim to study. For these reasons, we perform an additional check for clumps in the tails. Both the $\text{H}\alpha$ - and UV-selected tail clumps are matched with the corresponding catalogs of $\text{H}\alpha$ clumps detected with MUSE observations and described in Poggianti et al. (2019). If a match is found, the HST clump is validated; if not, the clump is validated only if either the redshift from the MUSE spectrum at the corresponding position of the clump is consistent with that of the galaxy or no redshift can be inferred from the MUSE spectrum but the clump is detected in all HST filters. To infer the redshift, emission lines such as the $[\text{N II}]$ 6548, 6583 – $\text{H}\alpha$ and $\text{H}\beta$ – $[\text{O III}]$ 4958, 5006 triplets and the $[\text{S II}]$ 6716, 6730 doublet are fitted to the MUSE spectra, obtained within a circular aperture as close as possible to that of the clump. After this selection, 73 $\text{H}\alpha$ and 216 UV candidates were rejected.

Finally, five UV-selected trunk clumps in the disks of JO201, JO204, JO206, and JW100 are removed, as their sizes and morphologies are such that they cannot be considered clumps, rather than more likely entire parts of the stellar disks.

For studying sizes, we define a subsample (resolved sample) of resolved clumps¹³ by selecting those objects whose PSF-corrected core radius, $r_{\text{core,corr}}$, exceeds the PSF FWHM ($0''.07$), which corresponds to ~ 140 pc at the typical redshifts of our targets.

Furthermore, when specified in the following, we removed regions whose emission is powered by an AGN. In order to do that, we used the BPT maps (Baldwin et al. 1981) of the MUSE images of the corresponding galaxies (Poggianti et al. 2017b). Adopting the boundary lines by Kauffmann et al. (2003), Kewley et al. (2001), and Sharp & Bland-Hawthorn (2010), the MUSE spaxels were flagged as star-forming, composite, AGN, or LINER regions according to the line ratios $\log([\text{N II}]/\text{H}\alpha)$ and $\log([\text{O III}]/\text{H}\beta)$ (for the spaxels with $\text{S/N} > 3$ for each line). The HST clumps are flagged as the MUSE spaxels they fall into, and in the following we remove those flagged as AGN or LINER when studying the luminosities of the $\text{H}\alpha$ -selected clumps.

4.3. Star-forming Complexes

The UV- and $\text{H}\alpha$ -selected clumps probe the emission coming from or due to stars younger than $\sim 10^8$ and $\sim 10^7$ yr, respectively. The contribution from stellar components older than such timescales can be detected in other optical bands used in this analysis in order to trace the entire stellar population formed from the stripped gas in the tails.

Therefore, we decided to also run ASTRODENDRO on the F606W filter images, which are deeper than the UV images (see Gullieuszk et al. 2023) and sensitive to older stellar populations with respect to F275W and $\text{H}\alpha$. Details of the ASTRODENDRO run on the F606W images are given in the Appendix. Only tail trunk clumps are considered, and we retain only F606W clumps overlapping with at least 1 pixel of any star-forming clump in either the $\text{H}\alpha$ - or UV-selected samples. In the following, we define a “star-forming complex” as the union of an F606W clump and each star-forming clump matched to it.

5. Number of Clumps: Disk, Extraplanar, and Tail Clumps

All of the clumps are shown in Figure 6 (the complete figure set is available in the online journal). Here the disk, extraplanar, and tail clumps can be seen in different colors, and their hierarchical tree structure can be appreciated from the color shading. In Figure 7, we show zoomed-in examples of $\text{H}\alpha$ -selected clumps in JO201 to illustrate the hierarchical structure and irregular morphologies of these clumps.

The largest clumps are found in the disks of JO175, JO201, and JO206 and the extraplanar region of JO206. As shown by Figure 7, large disk clumps (red contours) typically contain several subclumps (yellow contours), while extraplanar and especially tail clumps often have only one level. One can also appreciate the effects of RPS on extraplanar clumps, like the filamentary structures in JO206 and JW100, which are particularly bright in UV (bottom right panels in Figures 6.4 and 6.6).

In the tails, clumps are often aligned in extended linear or arched structures, suggesting the presence of many subtails in each galaxy (as already noticed in Bellhouse et al. 2021 and Franchetto et al. 2020, who found subtails in these galaxies from MUSE images). Whether clump and complex properties

¹³ When possible, we substitute unresolved leaf clumps with the smallest resolved parent branch clump if it does not contain another resolved leaf clump.

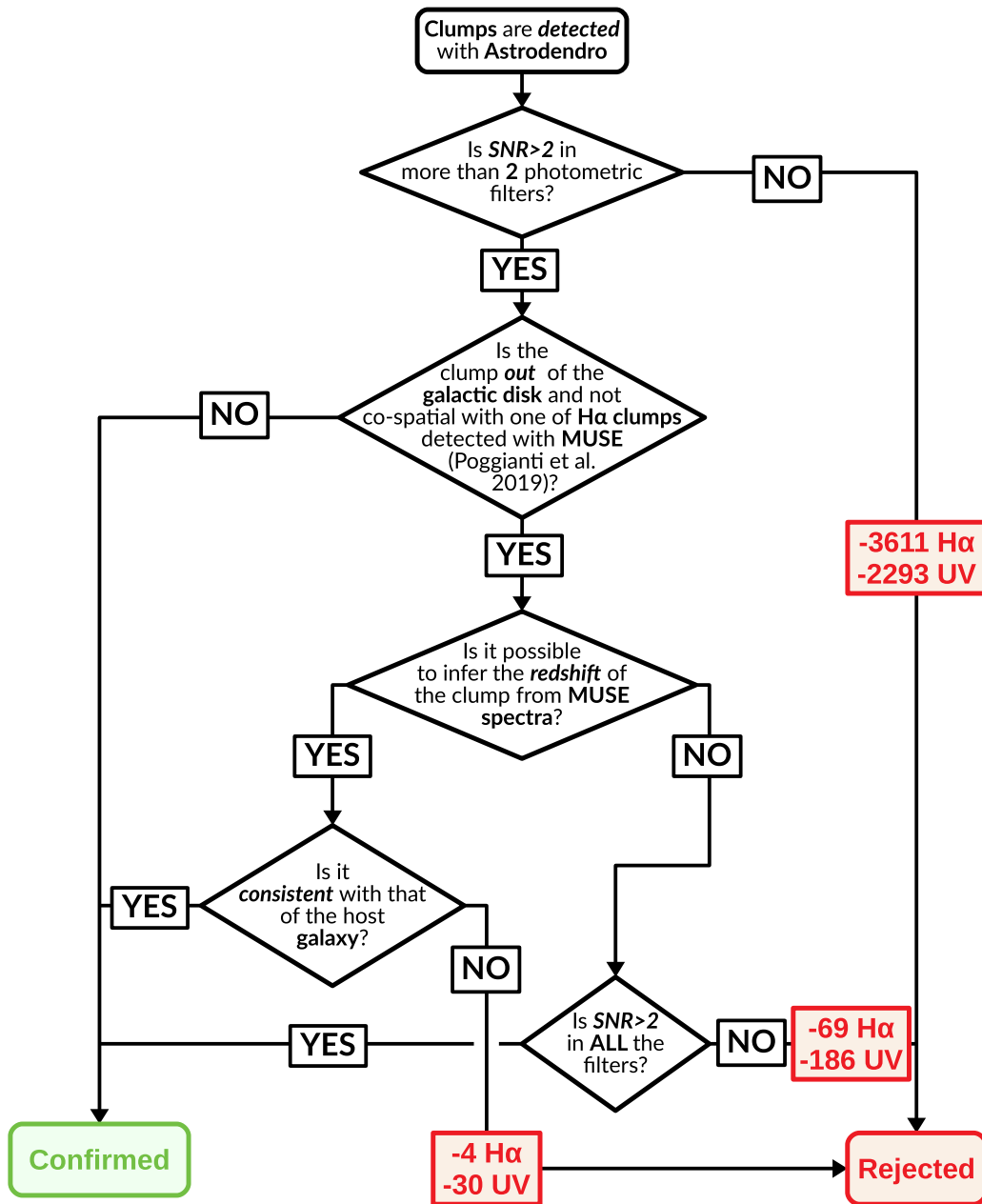


Figure 4. Flowchart summarizing the selection procedure adopted in this paper to confirm or reject clump candidates detected by ASTRODENDRO. For each step, we report in a red box the number of rejected H α - and UV-selected clumps.

correlate with distance from the galaxy or along its subtails and how they are influenced by the properties of the hosting galaxy are beyond the scope of this paper and will be investigated in future works.

Figure 8 shows a zoomed-in F606W image of some structures in the tails of JO201 to better appreciate the different spatial distributions of star-forming complexes (dark violet contours), H α -selected clumps (dark orange), and UV-selected clumps (magenta). Typically, an H α -selected clump has a corresponding UV-selected clump, while the opposite is not true. Indeed, the number of UV-selected clumps is higher than the number of H α -selected ones (see below). Furthermore, the corresponding UV-selected clump is generally bigger and almost completely encompasses the H α -selected clump. Similarly, star-forming complexes contain many UV- and H α -selected clumps embedded in fainter optical regions.

The number of star-forming clumps and complexes per galaxy is given in Tables 3 and 4, respectively. In total, including all galaxies, our LT sample comprises 2406 H α -selected clumps (1708 disk, 375 extraplanar, and 323 tail clumps), 3745 UV-selected clumps (2021 disk, 825 extraplanar, and 899 tail clumps) and 424 star-forming complexes. Typically, 98%–99% of the selected clumps are leaves (including simple trunks with no substructures inside), while the trunks containing leaves represent only 1%–2% of the whole sample (the fraction increases to 7%–14% when restricting the analysis to resolved clumps).

Avoiding AGN areas and including both resolved and unresolved clumps, $\sim 21\%$ of the H α -selected and $\sim 7\%$ of the UV-selected clumps get excluded. The percentage is smaller in the latter, indicating that UV-selected clumps are more preferentially located outside of AGN regions than H α -selected

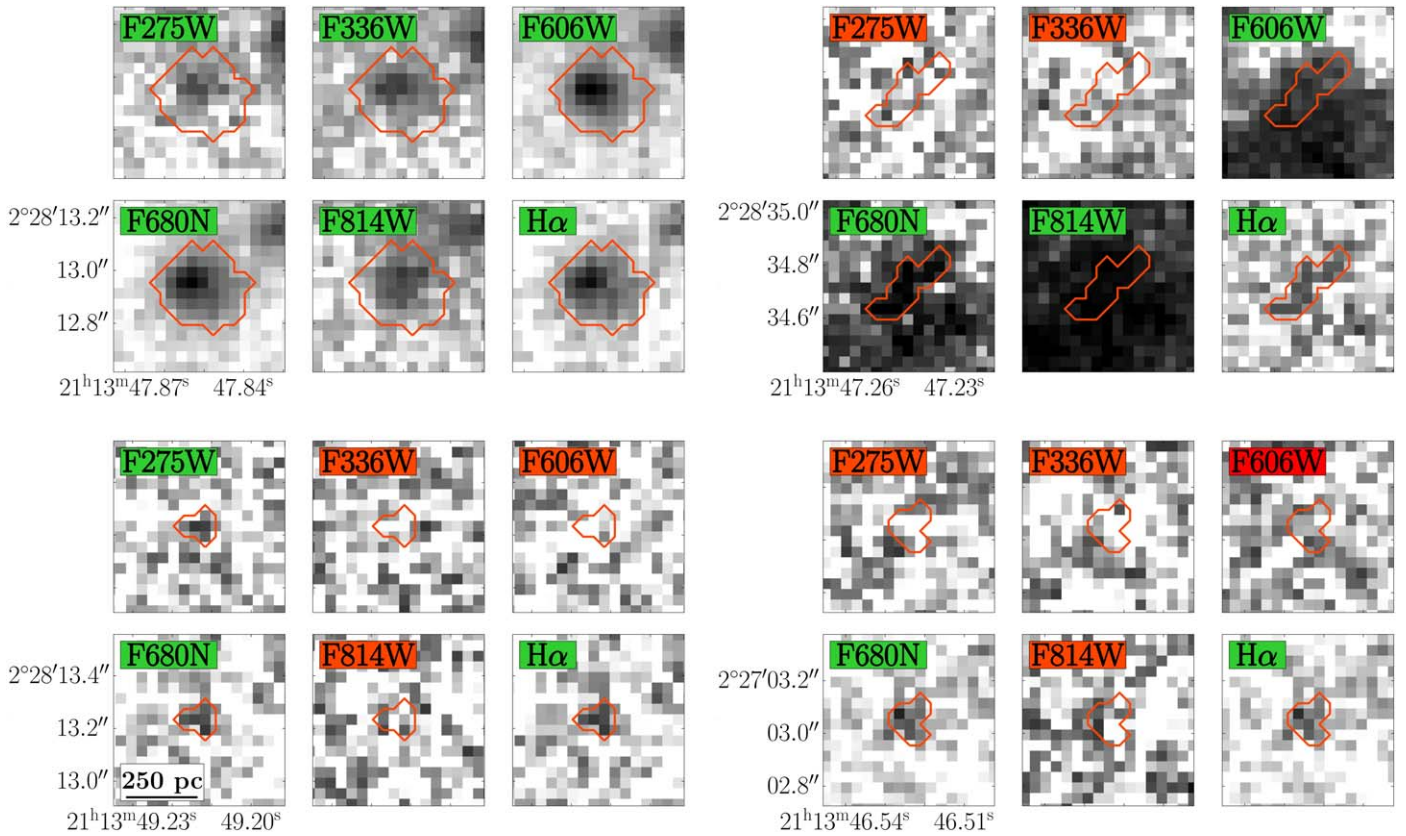


Figure 5. Images of four $H\alpha$ clumps of JO206 in all of the filters. Each clump is shown in six different filters (from top left to bottom right): F275W, F336W, F606W, F680N, F814W, and $H\alpha$. Each filter is labeled in green or red to show whether we have a detection or not, according to our definition (Section 4.2). The FOV is constant for all of the clumps (a length scale equal to 250 pc is plotted in the bottom left panel of the third clump).

clumps. Most of these are disk clumps, as expected, but a few of them can be found in the ionization cone of the AGN, whose extension can reach into the extraplanar region. The exact numbers are listed in parentheses in Table 3.

Only 12% of $H\alpha$ -selected and 16% of UV-selected clumps are spatially resolved, which means that the majority of the clumps have diameters smaller than ~ 140 pc. Most of the resolved clumps are star-forming according to the BPT, except in the disk, where about 25% of the $H\alpha$ -resolved clumps are flagged as AGN or LINER.

In Figure 9, we plot the histograms of the number of clumps per galaxy, divided according to the selection band ($H\alpha$ or UV) and spatial category (disk, extraplanar, or tail), together with the number of complexes.

In most cases, disk clumps are much more numerous than extraplanar and tail clumps regardless of the selection filter, with the only exception being the UV-selected clumps in JW100, which is seen edge-on and stripped mostly on the plane of the sky (Poggianti et al. 2019) and thus in the most favorable conditions to appreciate the extraplanar clumps. For what concerns the number of extraplanar and tail clumps, the prevalence of one over the other depends on the galaxy. In JW100, the number of extraplanar clumps is much larger than that of tail clumps in both selection filters; in JO204 and JO206, they are almost the same; and in the other galaxies, tail clumps are more numerous than extraplanar. The number of clumps in each category clearly depends on both the disk inclination and the stripping direction with respect to the line of sight.

Furthermore, with the only exception being disk clumps in JO175, for the same spatial category, there are more UV-

selected clumps than $H\alpha$ -selected ones. This indicates that there are a number of stellar-only clumps with little or no ionized gas left.

The number of star-forming complexes in the tails of the galaxies is generally smaller than the number of tail UV-selected clumps but larger than that of tail $H\alpha$ -selected ones, with the only exception being JO206, suggesting that many complexes are matched only to UV-selected clumps without any $H\alpha$ counterpart.

6. Distribution Functions

The LDF and SDF are defined as the number of sources per luminosity (size) bin normalized by the width of the luminosity (size) bin itself and by the total number of sources in the sample and is a useful tool to study the statistical properties of the star-forming clumps. As described in Section 1, they are typically well described by a power law and seem to be good proxies of the environmental effects on the star formation process and the clustering properties of the clumps.

6.1. Luminosity Distribution Functions

Figures 10 and 11 show the histograms of the clumps in each spatial category and galaxy binned in luminosity. The y-axes of the plots are normalized by the total number of clumps in the spatial category and galaxy. Most $H\alpha$ -selected clump distributions are peaked at values fainter than $\sim 10^{38}$ erg s $^{-1}$, at the faint end of the luminosity dynamical range. The luminosities of the $H\alpha$ -selected clumps are consistent with those of “giant” H II regions (like the Carina Nebula), whose $H\alpha$ luminosities $L(H\alpha)$ are typically 10^{37-39} erg s $^{-1}$, and “supergiant” H II

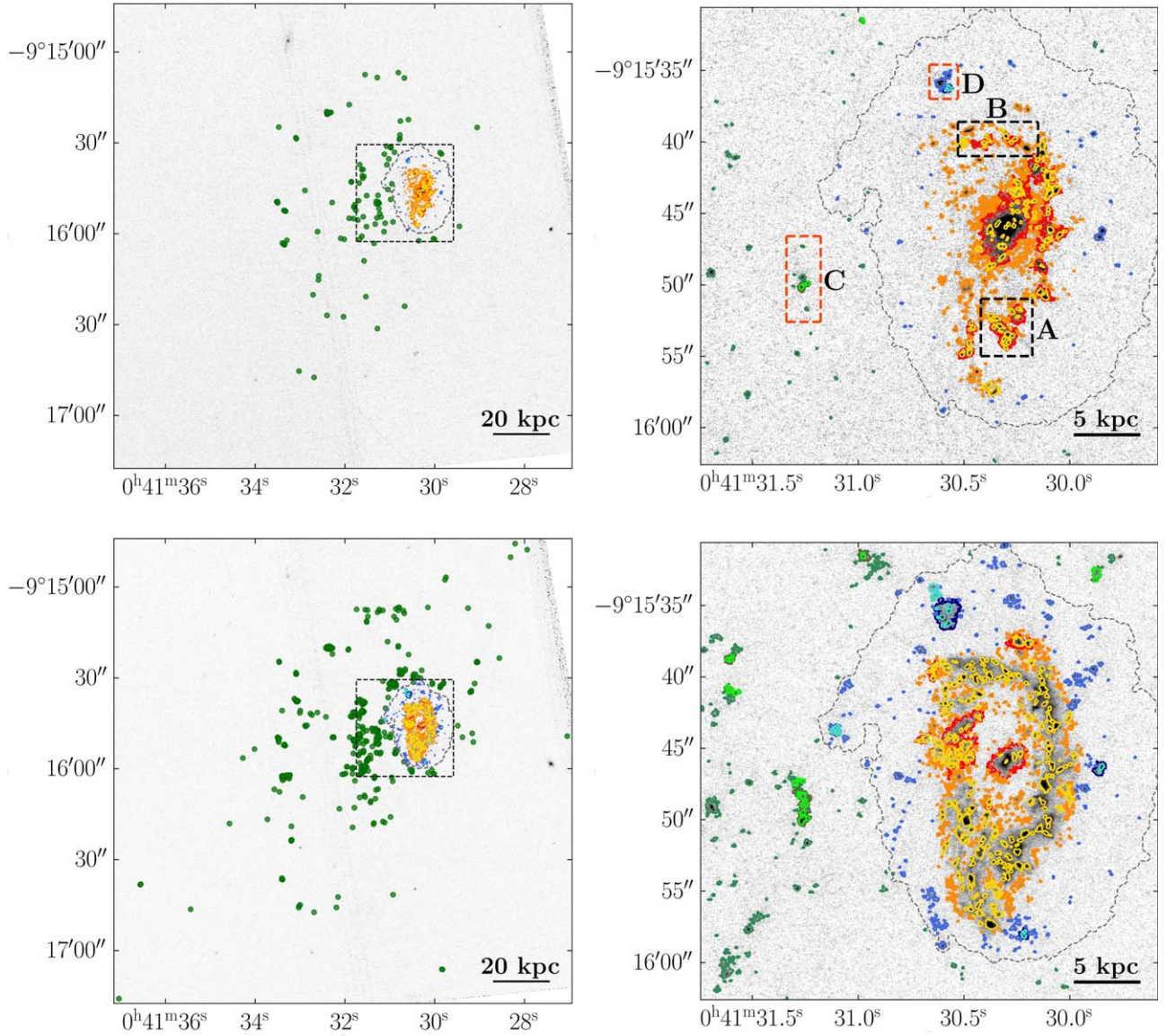


Figure 6. Map of the clumps detected in JO201, superimposed onto the image in the filter used for the detection. Top panels: $H\alpha$ -selected clumps. Bottom panels: UV-selected clumps. Left panels: FOV including all clumps. Right panels: zoomed-in version on the vicinity of the disk (highlighted in the left panel with the black dashed rectangle). Colors in the right panels represent the spatial category and tree structure (Sections 3 and 4.1); disk clumps are plotted in red (trunks that are not leaves), orange (trunks that are leaves), and yellow (leaves that are not trunks). Similarly, extraplanar clumps are plotted in dark blue, medium blue, and light blue and tail clumps are plotted in dark green, medium green, and light green in the right panels. The gray dashed contour is the galaxy disk contour (see Section 3). In the left panels, for the sake of clarity, the tail clumps are plotted as green dots of fixed size. The regions highlighted and labeled as A, B, C, and D are shown in Figure 7. (The complete figure set (6 images) is available.)

regions (like 30 Doradus in the Large Magellanic Cloud), with $L(H\alpha) > 10^{39}$ erg s $^{-1}$ (Lee et al. 2011). As expected, the faintest clumps are observed mostly in the closest galaxies of our sample (Table 1). Object JO201 stands out for its population of bright $H\alpha$ -selected clumps in both the disk and the tail, while in the extraplanar regions, the brightest clumps are those of JO206 (located in the crest to the top right of the disk; see Figure 6.4). Similar trends are found for UV-selected clumps. Also, we point out the hint of a bimodality in the distributions of the disk UV-selected clumps of JO201 and JW100 and the extraplanar clumps of JO206. Finally, the star-forming complex distributions are very different from the others, since they do not peak at the faint end of the distribution.

As done in Cook et al. (2016), throughout this work, the data points of the LDFs $d\tilde{N}/dL$ are computed by fixing the number of objects while varying the bin size in order to obtain a robust representation of the distribution function. For our LDFs, we choose 20 sources bin $^{-1}$. The luminosity of each bin is the central luminosity of the bin. Data points brighter than a given peak luminosity L_{peak} are fitted¹⁴ by a power law,

$$p(L) = K L^{-\alpha} \quad \text{with } L \geq L_{\text{peak}}, \quad (2)$$

¹⁴ Varying the number of clumps per bin between 5 and 50, the slope of the fit to the LDF does not change significantly. When using a different fitting method that does not depend on the binning (POWERLAW; Clauset et al. 2009; Klaus et al. 2011; Alstott et al. 2014), the results do not change significantly either.

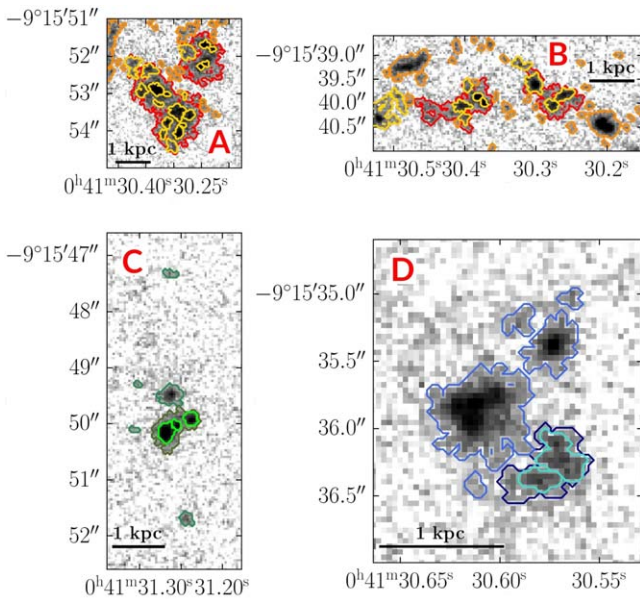


Figure 7. The $H\alpha$ images of the JO201 regions highlighted in the top right panel of Figure 6. The colors are the same as in Figure 6.

where K is the normalization, and α is the slope of the power law. The L_{peak} is chosen for each subsample starting from the peak value of the LDF and, if necessary, varying it in order to avoid noisy regions of the LDF.

The $H\alpha$ -selected clumps, UV-selected clumps, and star-forming complexes are fitted independently in each spatial category in order to study variations in the properties of the LDFs as a consequence of RPS. We used the whole UV-selected and star-forming complex samples but only the BPT-selected $H\alpha$ -selected clumps in order to avoid AGN- and LINER-powered regions (see Section 4.2). Fits were performed using the CURVE_FIT method implemented in the SCIPY¹⁵ Python package, with uncertainties on the LDF computed as the Poisson noise of the number of objects in the bin.

In Figures 12 and 13, we plot the observed LDFs together with the corresponding best-fitting power laws. Tail LDFs seem to be well described by a single power law for both $H\alpha$ - and UV-selected clumps.

In Table 5, we list the best-fitting values of the slopes α and normalizations K together with the peak luminosities L_{peak} . Considering all of the cases, the value of the slope α is in the range from 1.61 to 1.88 (thus always smaller than 2), with a mean value of 1.79 ± 0.09 (1.84 ± 0.03 for $H\alpha$ -selected clumps and 1.73 ± 0.09 for UV-selected clumps). In order to rule out the possibility that the inclusion in the sample of trunk clumps with subclumps can bias the results, we performed the same fits to the LDFs excluding them. Since this kind of trunk is $\sim 2\%$ of the whole sample, excluding them does not significantly affect the results, and the leaf-only slopes are always consistent within 1σ with those obtained including both trunks and leaves.

Our LDF slopes are consistent with previous results for H II regions (2.0 ± 0.5 ; Kennicutt et al. 1989) and smaller than 2. Similar results have been found by Santoro et al. (2022) for H II regions and Cook et al. (2016) for UV-selected young stellar clusters.

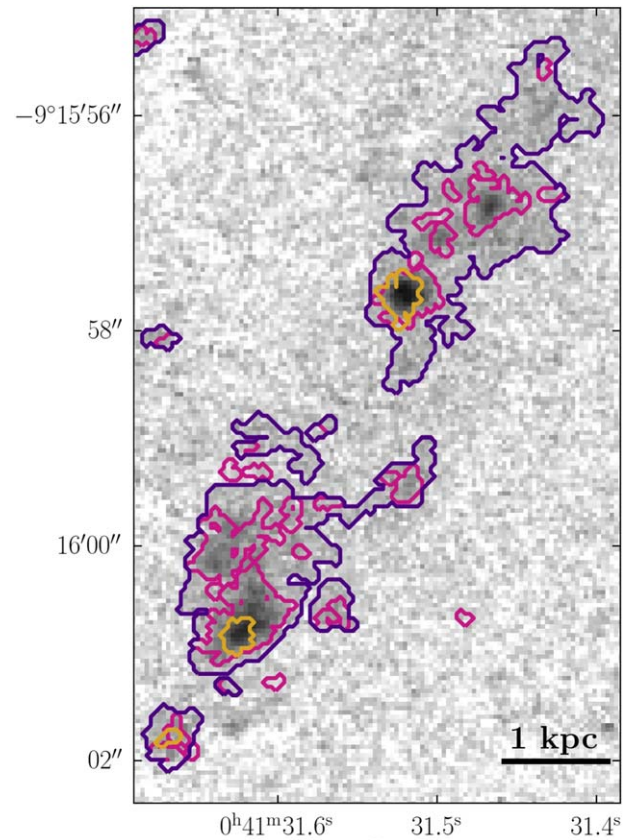


Figure 8. Zoomed-in F606W image of some star-forming complexes and clumps in JO201. The $H\alpha$ -selected clumps are plotted in dark orange, UV-selected clumps in magenta, and complexes in dark violet.

We also performed a Kolmogorov–Smirnov (K-S) test on the luminosity distributions for pairs of spatial categories for $H\alpha$ - and UV-selected clumps separately to infer whether the LDF significantly changes from one region to another. We compare the distributions above the maximum L_{peak} value above which we can assume all three subsamples to be complete. The resulting P values are listed in the Appendix (Table A2) and consistent with what one would expect when comparing the slopes of the LDFs. For $H\alpha$ -selected clumps, where the slopes are consistent with each other within the errors, the K-S test cannot exclude that each pair of distributions is identical. For UV-selected clumps, the K-S test confirms significant differences for the pairs disk–extraplanar and disk–tail.

In the top panel of Figure 14, we show the comparison among the best-fitting slopes as a function of the selection band and spatial category. Both the UV and $H\alpha$ slopes steepen going from disk to extraplanar to tail regions, where the closest match with the expected slope $\alpha = 2$ is found.

Shallower LDFs are found in galaxies with high specific SFR (sSFR; Santoro et al. 2022), such as all of our jellyfish galaxies (Vulcani et al. 2018), which may explain why our slopes are smaller than 2. Furthermore, as described in Section 1, past works (Cook et al. 2016; Messa et al. 2018; Santoro et al. 2022) find flatter LDFs in environments with a high SFR surface density Σ_{SFR} . Whether tails and disks are characterized by different Σ_{SFR} is a matter of future work, where masses and SFRs of the clumps will be found by SED fitting. Projection effects and blending, which are more likely to affect the disk than the tails, have also been demonstrated to

¹⁵ <https://docs.scipy.org/doc/scipy/index.html>

Table 3
Number of Clumps in Each Subsample

Filter (1)	Gal. (2)	LT Sample				Resolved Sample			
		N_{LT} (3)	N_d (4)	N_e (5)	N_t (6)	n_{res} (7)	n_d (8)	n_e (9)	n_t (10)
H α	JO175	290(290)	252(252)	14(14)	24(24)	38(38)	37(37)	0(0)	1(1)
	JO201	663(476)	507(321)	51(49)	105(105)	115(88)	96(69)	4(4)	15(15)
	JO204	373(296)	290(219)	44(38)	39(39)	40(30)	32(23)	5(4)	3(3)
	JO206	438(377)	234(173)	117(117)	87(87)	44(37)	24(17)	19(19)	1(1)
	JW39	235(168)	192(125)	4(4)	39(39)	14(12)	11(9)	0(0)	3(3)
	JW100	407(284)	233(139)	145(116)	29(29)	35(18)	24(9)	9(7)	2(2)
	Total	2406(1891)	1708(1229)	375(339)	323(323)	286(223)	224(164)	37(34)	25(25)
UV	JO175	287(287)	211(211)	17(17)	59(59)	47(47)	38(38)	2(2)	7(7)
	JO201	1244(1100)	659(518)	213(209)	372(372)	233(211)	143(122)	29(28)	61(61)
	JO204	531(475)	302(258)	110(102)	119(115)	82(78)	63(59)	9(9)	10(10)
	JO206	741(733)	392(384)	186(186)	163(163)	106(104)	51(49)	41(41)	14(14)
	JW39	355(349)	243(237)	6(6)	106(106)	31(31)	26(26)	0(0)	5(5)
	JW100	587(533)	214(178)	293(274)	80(80)	92(78)	48(36)	37(35)	7(7)
	Total	3745(3476)	2021(1787)	825(794)	899(895)	591(549)	369(330)	118(115)	104(104)

Note. Number of clumps detected in each galaxy and depending on the spatial category. The columns are (1) photometric band in which the clumps were detected, (2) name of the galaxy, (3) number of LT clumps, (4) number of disk LT clumps, (5) number of extraplanar LT clumps, (6) number of tail LT clumps, (7) number of resolved clumps, (8) number of resolved disk clumps, (9) number of resolved extraplanar clumps, and (10) number of resolved tail clumps. Parentheses enclose the number of clumps in each sample selected in order to avoid regions powered by AGN emission (see Section 4.2).

Table 4

Number of Star-forming Complexes Detected in the Tails of Each Galaxy

Gal.	N
JO175	31
JO201	129
JO204	53
JO206	92
JW39	73
JW100	46
Total	424

flatten the LDF (as demonstrated by Dessauges-Zavadsky & Adamo 2018 in the case of a mass distribution function). Flatter slopes are also found in simulations that include the aging effect of the most massive clumps (Gieles 2009; Fujii & Portegies Zwart 2015), which would be consistent with the fact that the slopes of the H α -selected clumps (circles in Figure 14) are larger than those of the UV-selected clumps (squares) of the corresponding spatial category. It would also be confirmed by the slope of the star-forming complexes (all of which are located in the tails by construction), which is very close to that of the tail UV-selected clumps.

Our analysis therefore suggests that the tails contain proportionally fainter clumps than the disks, and the extraplanar regions are intermediate between the two. However, this difference is statistically significant only when comparing UV-selected disk clumps with the other spatial categories, while for H α -selected clumps, there are only hints of such a trend (Figure 14). Furthermore, observational biases could explain the shallower LDF observed in disk clumps, since disk clumps are expected to be more affected by blending effects and underlying disk contamination, while the tail clumps are the least contaminated population, being isolated. Hence, their observed LDF should be the closest to the intrinsic one. Indeed,

it is the closest to the theoretical expected value of 2 (Elmegreen 2006). Thus, we can conclude that the properties of the gas in which clumps are embedded are likely to play a minor role in influencing the LDF. Nonetheless, this analysis cannot fully exclude effects on other properties of the clumps, like the mass, which we will investigate in future works.

6.1.1. Deviation from Single Power Law

Carefully inspecting Figure 12, it is evident that disk (and, to some extent, extraplanar) LDFs show some particular features, such as slope changes, plateaus, and secondary peaks, hinting at the need for a more complex model rather than a single power law. To characterize these different regimes, disk LDFs are divided into three intervals, the faint-end interval, the plateau, and the bright-end interval, each fitted with a power law. Furthermore, for the H α -selected LDF, we also fit a power law to the data points brighter than 1.2×10^{39} erg s $^{-1}$, corresponding to a secondary peak of the LDF¹⁶ (hereafter the “secondary-peak interval”). We superimposed the best-fitting disk power laws on the extraplanar LDFs in order to understand if this spatial category could also be characterized by the same regimes (we do not have enough statistics to divide the extraplanar LDFs into intervals and fit a power law in each of them).

The best-fitting slopes and the luminosity range boundaries of each interval are shown in Table 6, and in Figure 15, we show the best-fitting power laws superimposed onto the disk and extraplanar LDFs.

Concerning H α -selected LDFs, the faint-end interval slope is larger than that of the bright-end interval, hinting at a change in

¹⁶ This secondary peak is dominated by clumps in JO201 (the galaxy with the largest number of disk and tail clumps). Nonetheless, we do not have reason to think there is a bias in luminosity artificially increasing the number of clumps at such luminosity; therefore, it is a matter of interest to characterize this interval, too.

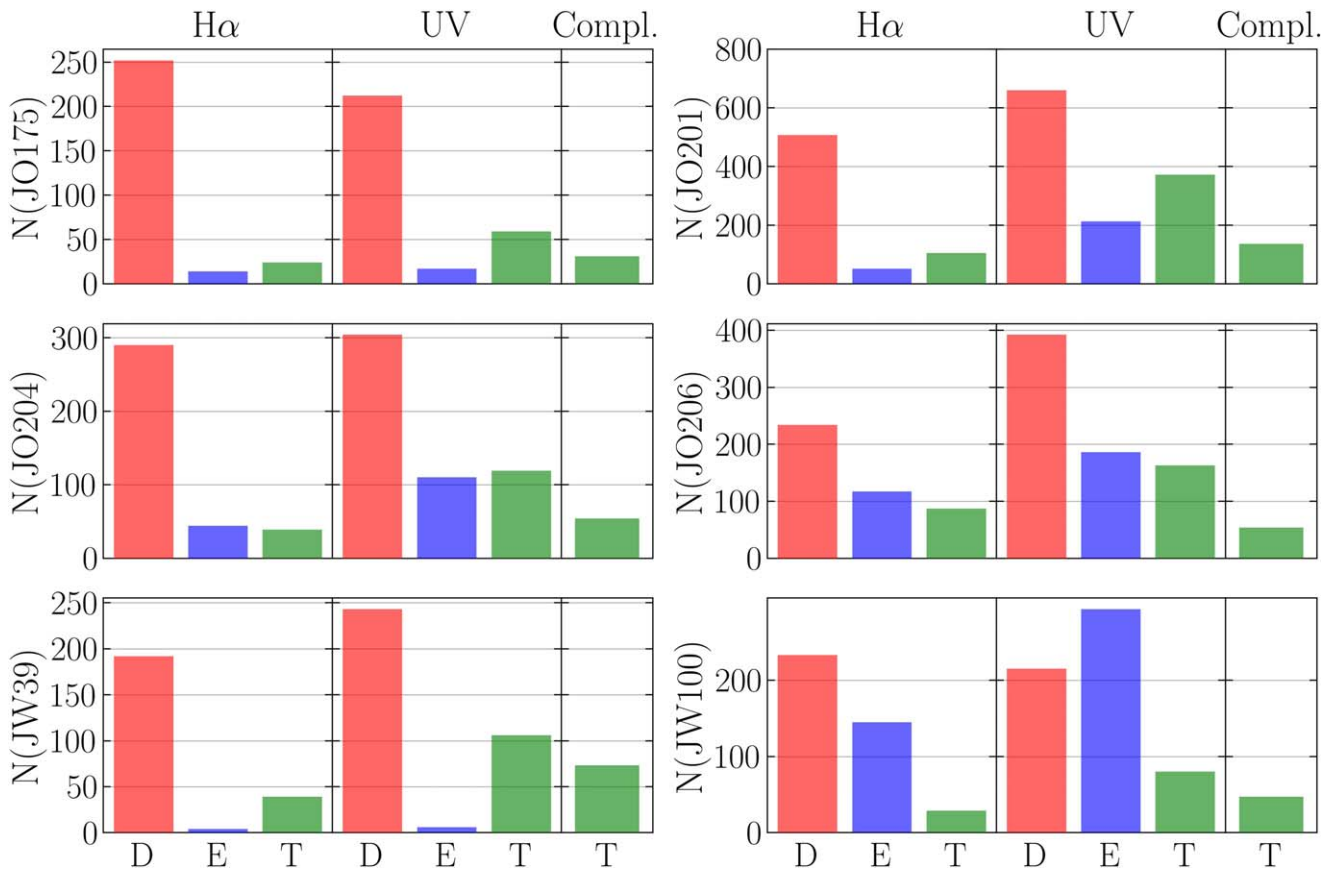


Figure 9. Histograms of the number of star-forming clumps and complexes in each galaxy, divided according to the selection filter and spatial category. For each galaxy, three panels are shown, with the number of H α -selected clumps (left panel), UV-selected clumps (middle panel), and star-forming complexes (right panel) divided according to their spatial category: disk (red), extraplanar (blue), and tail (green).

the properties of the clumps before and after the plateau. When considering the secondary-peak interval, the distribution gets steeper than for the bright-end interval but is still flatter than at the faint end. When superimposing these results on the extraplanar LDF (right panels in Figure 15), we can notice that the faint- and bright-end best-fitting power laws describe the distribution quite well. On the other hand, the extraplanar LDF seems to lack the plateau and secondary peak, even though we do not have enough data points in these intervals to exclude this hypothesis.

Concerning the disk UV-selected LDF, the slopes in the faint- and bright-end intervals are consistent within the uncertainties. The plateau covers a wider luminosity range compared to the H α plateau. The presence of a plateau in UV LDFs has never been observed before. Furthermore, the extraplanar LDF is well described by the results obtained for the disk, especially in the faint-end interval.

Whether these different regimes are an effect of aging or not is not clear yet. The position of the plateau in the disk H α LDF is compatible with a change in the bounding regime (from density-bound to ionization-bound) of the H II regions (Beckman et al. 2000) at a predicted H α luminosity (at $\sim 4 \times 10^{38}$ erg s $^{-1}$). On the other hand, the slopes at the low- and high-luminosity ends are similar, while the Beckman et al. (2000) model predicts a steepening at bright luminosities, where H II regions are ionization-bound. Moreover, our LDFs show the same plateau in the disk UV-selected clumps, which should not be affected by the change in the ionization regime.

6.2. Size Distribution Functions

In this section, we use the clumps of the resolved sample(s). The analysis of the SDF of the clumps is performed in the same way described in Section 6.1. The samples are binned using 15 sources bin $^{-1}$ for disk clumps and five sources bin $^{-1}$ for extraplanar and tail clumps because of the low number of clumps in these spatial categories. The SDFs are qualitatively similar to the LDFs. Their intrinsic functional form is a power law, but incompleteness effects introduce a cutoff at small sizes. In analogy with what we did for the LDF (Equation (2)), we define the peak value as size $_{\text{peak}}$, and we fit a power law to data points above this value.

In Figure 16, the observed SDFs and the best-fitting model of each subsample are shown. For completeness, we also plot the SDF data points of unresolved clumps, for which we have only upper limits for the sizes (filled circles). In order to do that, SDFs are not normalized for the total number of clumps, since the normalization changes when considering unresolved clumps or not. A single power law is likely to be a good representation of the resolved data, especially considering that the sample is about 15% of the one used to constrain the parameters of the LDFs (see Table 3). The loss of statistics can especially affect the extraplanar and tail subsamples, for which the regime in which the sample is complete includes just a few data points. The fitted power laws do not seem to well describe the unresolved data points, as expected from incompleteness. These features, together with the fact that unresolved clumps

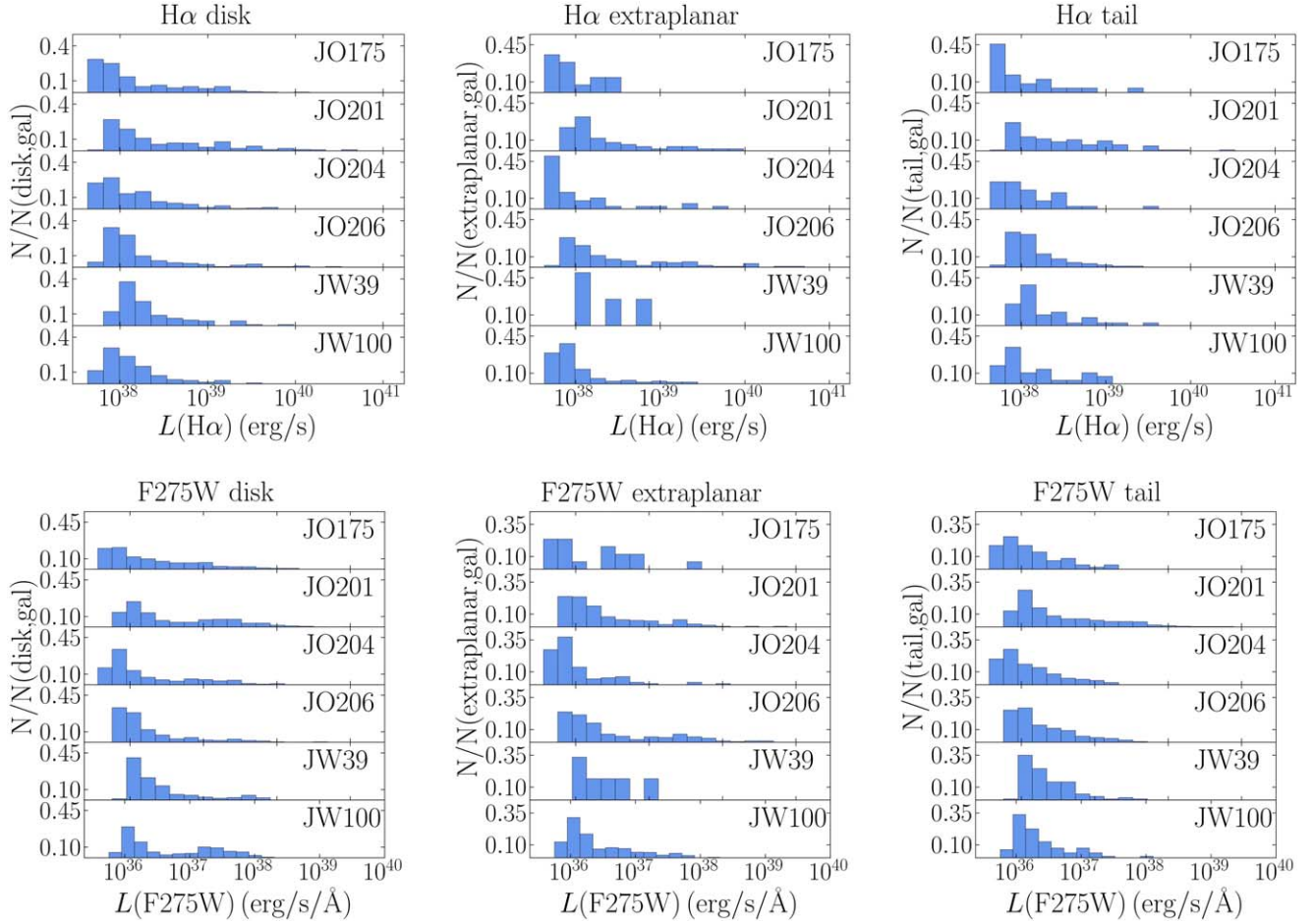


Figure 10. Fraction of H α - (top row) and UV- (bottom row) selected clumps per spatial category and galaxy. In each row, from left to right, we show disk, extraplanar, and tail. The y-axis is normalized for the number of clumps in the galaxy and spatial category. Notice that the H α luminosity of the H α -selected clumps is the integrated emission of the H α line and therefore in erg s^{-1} , while the UV luminosity of the UV-selected clumps is in $\text{erg s}^{-1} \text{\AA}^{-1}$.

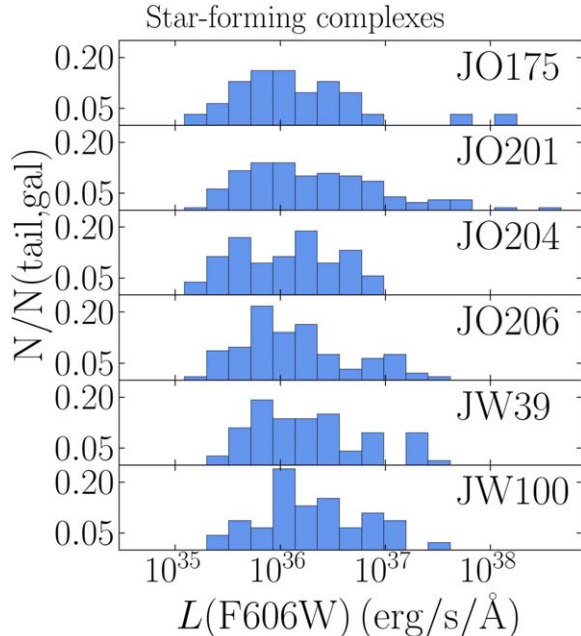


Figure 11. Same as Figure 10 but for star-forming complexes.

have, by definition, no reliable estimates of their sizes, imply that we cannot draw any conclusion for sizes below ~ 140 pc.

The best-fitting slopes and normalizations and the chosen size_{peak} of each subsample are listed in columns (6)–(8) of Table 5. The average slope is 3.3 ± 0.6 (3.6 ± 0.6 for H α -resolved clumps and 3.1 ± 0.3 for UV-resolved clumps). The slopes of the extraplanar and tail H α -resolved clumps are consistent with the one found by Kennicutt & Hodge (1980) in the disk of a low- z spiral galaxy ($\alpha = 4.1$).

As was done in Section 6.1 for LDFs, we computed the P values from the K-S statistics, comparing the size distributions of pairs of spatial categories and keeping the two selection filters separated. The results are listed in the Appendix (Table A2). In this case, the K-S finds significantly different distributions for all pairs, except for disk versus tail H α -resolved clumps. However, both the slopes and the P values have to be taken with caution due to small numbers, especially in the tail clumps.

We find that these distributions are different from those inferred for the H α clumps of these galaxies detected by Poggianti et al. (2019) from the MUSE H α luminosities using the luminosity–size relation by Wisnioski et al. (2012), where the expected median size was 440 pc for clumps in the disks

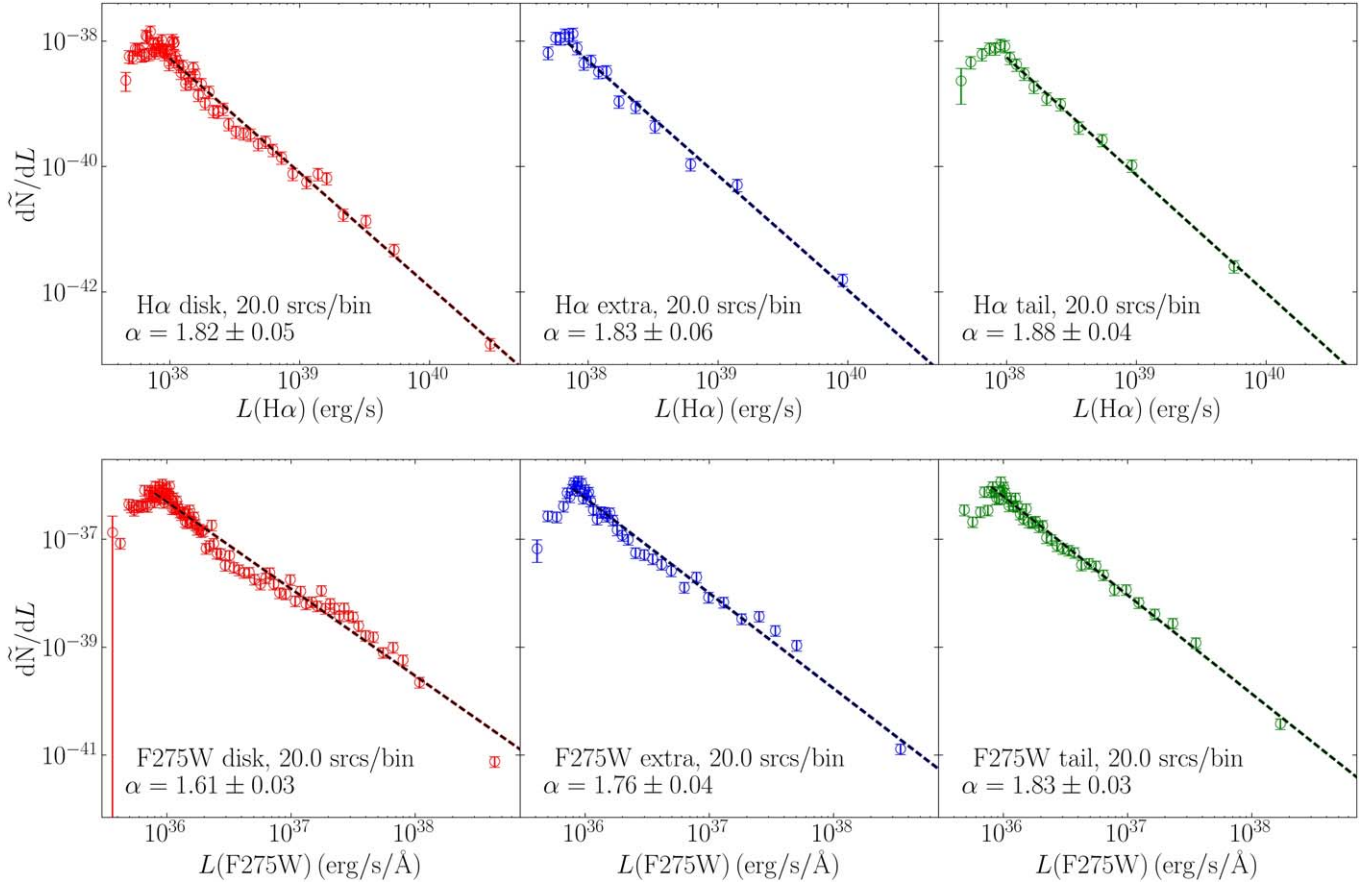


Figure 12. The LDFs $d\tilde{N}/dL$ of H α - (upper panels) and UV- (lower panels) selected clumps. Clumps are divided according to their spatial category: disk (left panels; red), extraplanar (middle panels; blue), and tail (right panels; green). For each plot, we show the empirical LDF of the corresponding sample (open circles with error bars) generated with equal-number bins (i.e., each bin contains the same number of objects; see Cook et al. 2016) and the best-fitting line (dashed line). Notice that the H α luminosity of the H α -selected clumps is the integrated emission of the H α line and therefore in erg s^{-1} , while the UV luminosity of the UV-selected clumps is in $\text{erg s}^{-1} \text{Å}^{-1}$.

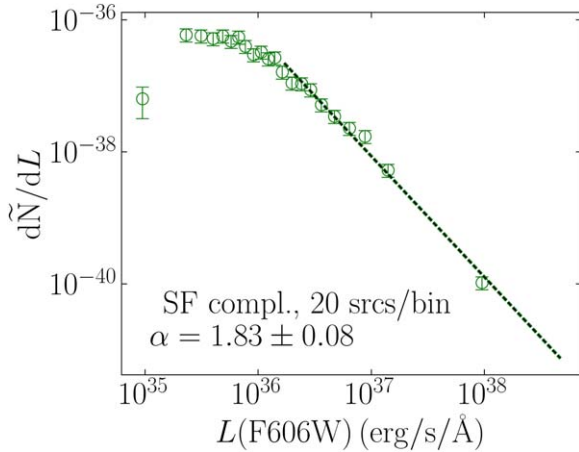


Figure 13. Same as Figure 12 but for star-forming complexes.

and 320 pc for clumps in the tails. Here the median sizes are ~ 210 , ~ 211 , and ~ 180 pc for disk, extraplanar, and tail H α -resolved clumps, respectively, and ~ 215 , ~ 223 , and ~ 208 pc for disk, extraplanar, and tail UV-resolved clumps. Consistent with what was inferred by Poggianti et al. (2019), the clumps in the tails are smaller than those in the disk. Nonetheless, the values found in this work are about half the expected size. The origin of this difference is a direct consequence of the

differences between the luminosity–size relation by Wisnioski et al. (2012) and the one obtained from our HST observations (see Section 7).

In the bottom panel of Figure 14, the slopes of the resolved clumps in each category are plotted. Also, in the case of SDFs, the slopes of UV-resolved clumps are smaller (with the exception of disk clumps), even if consistent within the error bars, than those of H α -resolved clumps. Moreover, disk and extraplanar UV-resolved slopes are almost equal, while in H α , there are hints of a slope increase from disk to tail regions.

The slope increase can be partially explained based on the work in Gusev (2014), whose observations of the nearby galaxy NGC 628 demonstrated that the overall slope of SDFs reaches values between 4.5 and 6¹⁷ when analyzing the smallest structures of the star-forming regions (i.e., what we define as leaves in Section 4.1) or isolated objects. Instead, the slope decreases up to 2.5 once all of the substructures of complex star-forming regions are taken into account. Our trend is analogous. We find steep slopes ($\sim 4.4 \pm 0.8$, consistent with 4.5) in the H α tails, whose clumps typically have no or few substructures. On the other hand, the slope is smaller in the case of disk clumps, which are more structured than extraplanar and tail clumps. Therefore, including both trunks and leaves in

¹⁷ Gusev (2014) studied the slopes of the cumulative distribution functions. Also, their slopes are defined as negative. Therefore, the slopes in this work (α_s) and the slopes by Gusev (2014; α_G) are connected by $\alpha_s = 1 - \alpha_G$.

Table 5
LDF and SDF Best-fitting Parameters

(1)	(2)	α	K_L	L_{peak} ($\text{erg s}^{-1} (\text{\AA}^{-1})$)	α_s	K_s	Size _{peak} pc
(1)	(2)	(3)	(4)	(5)	(6)	(7)	(8)
H α	D	1.82 ± 0.05	30.9 ± 1.8	1×10^{38}	2.8 ± 0.2	4.2 ± 0.4	150
	E	1.83 ± 0.06	31 ± 2	7×10^{37}	3.6 ± 0.6	6.4 ± 1.4	200
	T	1.88 ± 0.04	33.0 ± 1.6	1×10^{38}	4.4 ± 0.8	8 ± 2	160
UV	D	1.61 ± 0.03	21.8 ± 1.2	8×10^{35}	2.95 ± 0.16	4.6 ± 0.4	190
	E	1.76 ± 0.04	27.3 ± 1.6	8×10^{35}	2.9 ± 0.3	4.4 ± 0.7	200
	T	1.83 ± 0.03	26.9 ± 1.1	8×10^{35}	3.5 ± 0.4	5.9 ± 0.9	175
Complexes		1.83 ± 0.08	30 ± 3	1.7×10^{36}

Note. Best-fitting values of the LDFs and SDFs when fitted to the different samples of star-forming clumps and complexes. Column (1) refers to the clump selection photometric band. Column (2) gives, from top to bottom, disk (D), extraplanar (E), and tail (T) subsamples of H α - and UV-selected clumps; the last row refers to star-forming complexes, which are only in the tails by construction. Columns (3)–(5) contain the values of the best-fitting slopes α , the best-fitting normalization K_L , and the peak luminosity L_{peak} arbitrarily chosen, over which data points are fitted (Equation (2)). Notice that L_{peak} is in erg s^{-1} for H α -selected clumps, whereas it is in $\text{erg s}^{-1} \text{\AA}^{-1}$ for UV-selected clumps and star-forming complexes. Columns (6)–(8) list the same quantities (best-fitting slope α_s , best-fitting normalization K_s , and peak size size_{peak}) but for the SDFs.

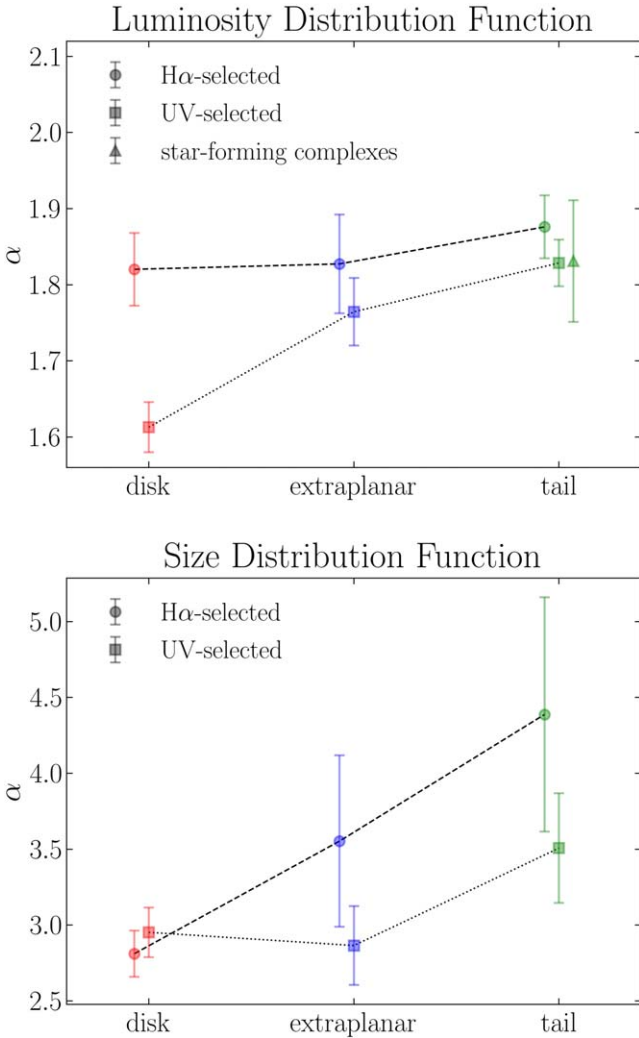


Figure 14. Comparison of the slopes of the LDFs (top panel) and SDFs (bottom panel) of star-forming clumps and complexes as a function of both the selection band and the spatial category (see Table 5). Circles are H α -selected clumps, squares are UV-selected clumps, and triangles are star-forming complexes. Colors refer to the spatial category: red for disk, blue for extraplanar, and green for tail.

the samples has little effect on the slope of tail clumps, while it may explain the flatter distribution found for disk clumps. Indeed, we observe steeper disk SDFs when using only the leaves (3.28 ± 0.28 in H α and 3.22 ± 0.23 in UV). Alternatively, recent simulations of star-forming regions in the presence of different ambient pressures (Nath et al. 2020) found slopes similar to the one of the disk SDFs, while they suggest the presence of a lower-pressure environment in the tail. The pressure producing the measured steepening in the tail SDF would be 1 order of magnitude lower than the typical ICM pressure of our galaxies (Bartolini et al. 2022). Therefore, the variation of the slope of the SDF across different environments seems to be different from that expected from environmental effects.

In conclusion, the largest clumps of our sample are found in the disk and extraplanar regions of our galaxies, whether we consider UV- or H α -resolved clumps, and (as hinted by the K-S test) clumps of different spatial categories are likely to follow different SDFs with different slopes. The sizes of the clumps seem to be poorly affected by the environment in which they are embedded, the ICM in the tails and ISM in the disks, and more linked to their clustering features.

7. Luminosity–Size Relations

In this section, we study the luminosity–size relation for both H α - and UV-resolved clumps. Here H α -resolved clumps are BPT-selected to avoid AGN- and LINER-powered regions. To calculate the linear regression fits with the inclusion of an intrinsic scatter, we employed the Python software package LINMIX (Kelly 2007). LINMIX implements a Markov Chain Monte Carlo algorithm to converge on the posterior and return a sample of sets of parameters drawn from the posterior distribution. The linear relation fitted by LINMIX is

$$\log L = m \log(\text{size}) + q + G(\varepsilon), \quad (3)$$

where L is the luminosity of the clump in the filter in which it is selected, size is the PSF-corrected core diameter, m is the angular coefficient of the correlation, q is the y-axis intercept, and $G(\varepsilon)$ is the intrinsic scatter computed from a Gaussian

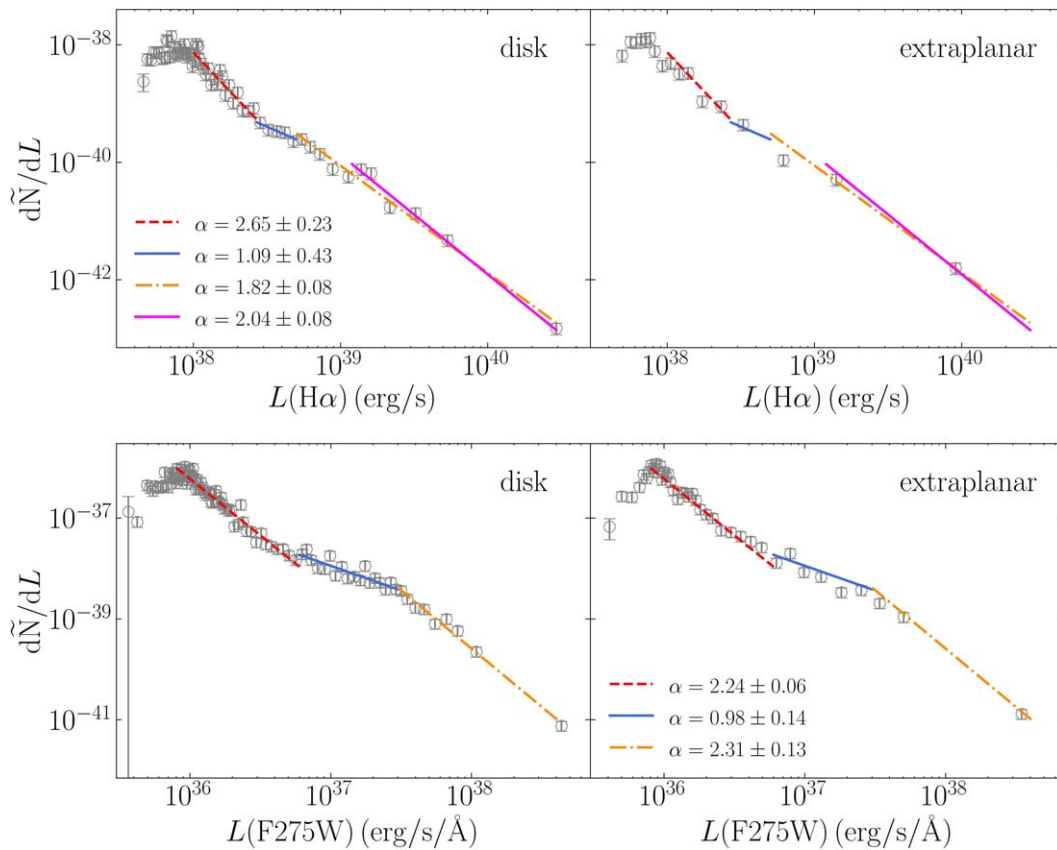


Figure 15. The LDFs \tilde{dN}/dL of H α - (upper panels) and UV- (lower panels) selected clumps. Clumps are divided according to their spatial category: disk (left panels; red), extraplanar (middle panels; blue), and tail (right panels; green). For each plot, we show the empirical LDF of the corresponding sample (open circles with error bars) generated with equal-number bins (i.e., each bin contains the same number of objects; see Cook et al. 2016) and the best-fitting line (dashed line). Notice that the H α luminosity of the H α -selected clumps is the integrated emission of the H α line and therefore in erg s^{-1} , while the UV luminosity of the UV-selected clumps is in $\text{erg s}^{-1} \text{ \AA}^{-1}$.

Table 6
Best-fitting Slopes to the Intervals of the Disk LDFs

Phot. Band	Parameters	Faint End	Plateau	Bright End	Secondary Peak
H α	α	2.7 ± 0.2	1.1 ± 0.4	1.82 ± 0.08	2.04 ± 0.08
	L_{\min} [erg s^{-1}]	1×10^{38}	2.7×10^{38}	5×10^{38}	1×10^{39}
	L_{\max} [erg s^{-1}]	2.7×10^{38}	5×10^{38}
UV	α	2.24 ± 0.06	0.98 ± 0.14	2.31 ± 0.13	...
	L_{\min} [$\text{erg s}^{-1} \text{ \AA}^{-1}$]	8×10^{35}	6×10^{36}	3×10^{37}	...
	L_{\max} [$\text{erg s}^{-1} \text{ \AA}^{-1}$]	6×10^{36}	3×10^{37}

Note. Results obtained when a set of power laws are fitted to the disk LDFs divided into intervals (Section 6.1). From left to right: clump selection photometric band, best-fitting slope α and luminosity range boundaries of the interval L_{\min} and L_{\max} , and names of the intervals.

distribution centered on $m \log(\text{size}) + q$ with standard deviation ϵ .

In Figure 17, we plot the data points in the $(\log L, \log(\text{size}))$ plane and the best-fitting lines for both H α - and UV-resolved clumps (left and right panel, respectively). Clumps are divided according to their spatial position.

The best-fitting parameters are listed in Table 7. The average slope is 2.3 ± 0.4 for H α -resolved and 1.97 ± 0.17 for UV-resolved clumps. The slopes for the disk and extraplanar H α -resolved clumps are consistent within 1σ and close to 2, while the slope for the tail clumps is steeper. In UV, the slopes of all spatial categories are consistent with each other.

The Strömgren sphere model predicts the slope to be 3 (Beckman et al. 2000), hinting that disk and extraplanar clumps are not well described by this model as a consequence of additional effects to be taken into account, such as RPS, transition from ionization-bound to density-bound, dust, metallicity, and magnetic fields (Wisnioski et al. 2012). On the other hand, Nath et al. (2020) obtained a slope equal to 2 simulating the expansion of ionized bubbles in a Milky Way-like ISM environment (in this case, H α -resolved tail clumps would be the only ones deviating from the prediction of the model). Cosens et al. (2018) proposed a model explaining why, in galactic disks, clumps with a low SFR surface density (Σ_{SFR})

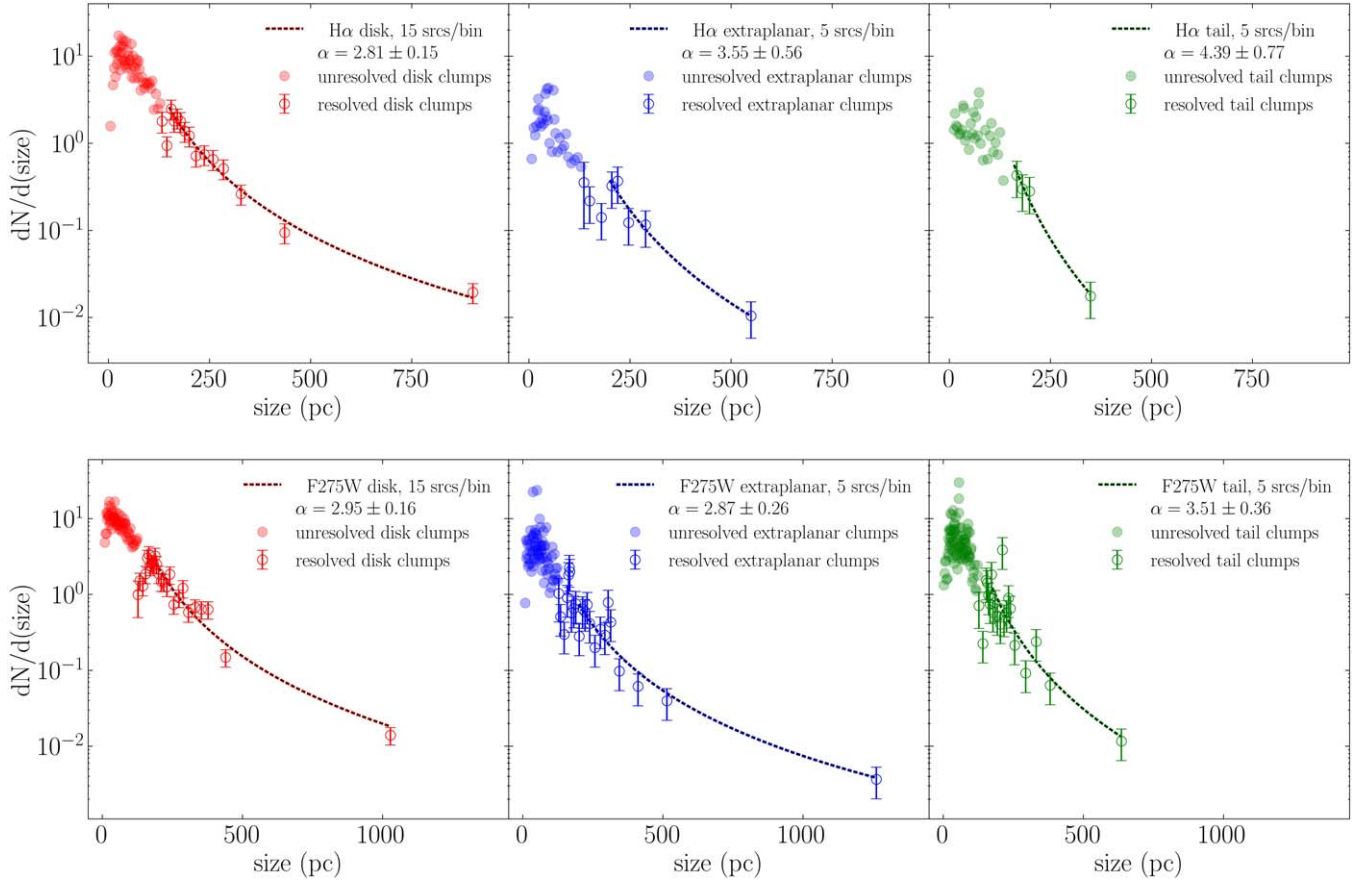


Figure 16. The SDFs for disk (red), extraplanar (blue), and tail (green) clumps. Top: $H\alpha$. Bottom: UV. Resolved clumps are shown as open circles with 1σ error bars, while unresolved clumps are plotted as filled circles without error bars. In this case, SDFs are not normalized by the total number of clumps, and the x -axis is in linear scale.

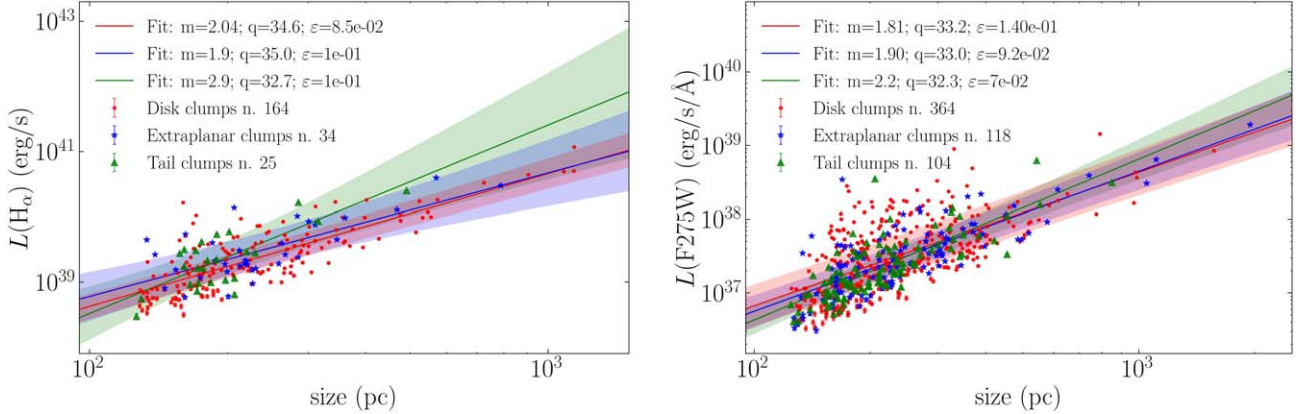


Figure 17. Luminosity–size relations for $H\alpha$ - (left) and UV- (right) resolved clumps. The clumps are plotted according to their spatial category: disk (red circles), extraplanar (blue stars), and tail (green triangles). The best-fitting lines to the three categories are plotted as solid lines of the corresponding color. The shaded areas are the uncertainties on the fits at 2σ . Note that $H\alpha$ luminosity is in erg s^{-1} , while F275W is in $\text{erg s}^{-1} \text{\AA}^{-1}$.

seem to follow a steeper relation (slope closer to 3) than clumps with high Σ_{SFR} (slope closer to 2). According to this model, if the expected radius of a Strömgen sphere is larger than the scale height of the disk (H), the ionized bubble can keep growing only across the galactic plane according to a power law with slope closer to 2 than 3. The flattening occurs only if the ionized region is brighter than a critical value. The fact that our slopes are consistent with 2 might therefore suggest that our clumps have an enhancement in the $H\alpha$ luminosity, maybe caused by RPS. Such a model would also explain why $H\alpha$ -

resolved tail clumps are likely to follow a steeper relation than clumps in the disk or extraplanar region. Tail clumps are embedded in the spherically symmetric ICM in place of the gaseous disk of the galaxy; therefore, they are not bound by H .

7.1. Comparison with Previous Results

In Figure 18, we compare the position of our $H\alpha$ -resolved clumps in $\log L - \log(\text{size})$ with those presented in the literature. We show results from Fisher et al. (2017), who

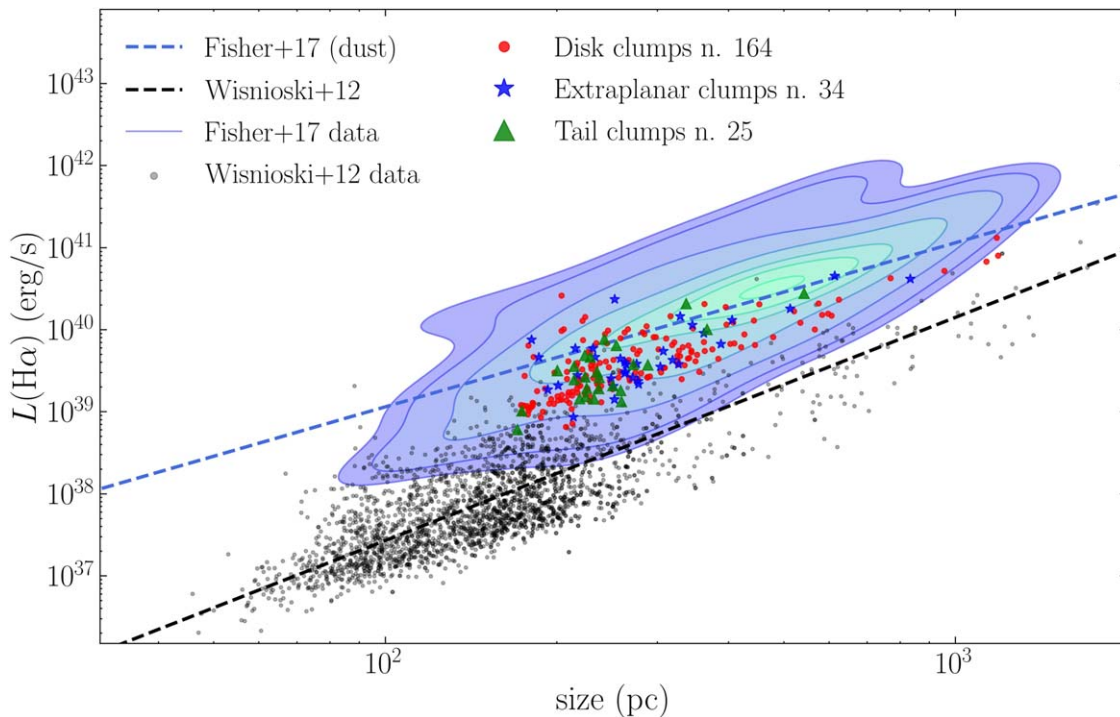


Figure 18. Shown is $\log(L(\text{H}\alpha)) - \log(\text{size})$ comparing our $\text{H}\alpha$ -resolved clumps with those in DYNAMO starburst galaxies (Fisher et al. 2017; blue contours) and local isolated star-forming galaxies presented in Wisnioski et al. (2012) (Gallagher & Hunter 1983; Arsenault & Roy 1988; Kennicutt et al. 2003; Rozas et al. 2006; Monreal-Ibero et al. 2007; black dots). Our clumps are plotted according to their spatial category: disk (red circles), extraplanar (blue stars), and tail (green triangles). Our clump luminosities and sizes are corrected in order to make the comparison more trustworthy; for the same reason, DYNAMO clump luminosities are corrected by reading the effects of dust extinction. The black dashed line is the best-fitting relation by Wisnioski et al. (2012), and the blue dashed line is obtained by fitting the dust-extinguished DYNAMO clumps and keeping the slope fixed at 2, as in Fisher et al. (2017). The clumps in our sample lie in between the two samples, being especially close to clumps in starburst galaxies.

Table 7
Luminosity–Size Relations Best-fitting Parameters

Spat. Cat. (1)	$\text{H}\alpha$			UV		
	m (2)	q (3)	ε (4)	m (5)	q (6)	ε (7)
Disk	2.04 ± 0.12	34.6 ± 0.3	$(8.5 \pm 1.0) \times 10^{-2}$	1.81 ± 0.12	33.2 ± 0.3	$(14.0 \pm 1.0) \times 10^{-2}$
Extraplanar	1.9 ± 0.4	35.0 ± 0.8	$(10 \pm 3) \times 10^{-2}$	1.90 ± 0.14	33.0 ± 0.3	$(9.2 \pm 1.3) \times 10^{-2}$
Tail	2.9 ± 0.5	32.7 ± 1.2	$(10 \pm 3) \times 10^{-2}$	2.2 ± 0.2	32.3 ± 0.4	$(7 \pm 1) \times 10^{-2}$

Note. Best-fitting parameters (m , q , ε ; with 1σ uncertainties) of the luminosity–size linear relations (Equation (3)) for $\text{H}\alpha$ - (columns (2)–(4)) and UV- (columns (5)–(7)) resolved clumps. Each spatial category (column (1)) is fitted separately.

studied clumps belonging to turbulent, extremely $\text{H}\alpha$ -bright DYNAMO galaxies, and those by Wisnioski et al. (2012), who studied $z \sim 0$ isolated star-forming galaxies (Gallagher & Hunter 1983; Arsenault & Roy 1988; Kennicutt et al. 2003; Rozas et al. 2006; Monreal-Ibero et al. 2007). We also show the best-fitting relations they presented in their works.

The luminosities of the DYNAMO clumps in Figure 18 were corrected by reading extinction caused by dust, since both our luminosities and those computed by Wisnioski et al. (2012) are not dust-corrected. Dust-extinguished DYNAMO clumps are then fitted to a power law with a slope fixed at 2, as in Fisher et al. (2017).

As described in detail in Fisher et al. (2017), the radii of the DYNAMO clumps were found by fitting a 2D Gaussian to the light distribution, with the addition of a constant representing the local background level (Fisher et al. 2017). To make the comparison with DYNAMO as consistent as possible, we

derive new PSF-corrected core radii (r_{Gauss}) by fitting a 2D Gaussian+constant to our tail $\text{H}\alpha$ -resolved clumps, which are more isolated and in a fainter local background than the disk and extraplanar clumps. We then visually select only clumps for which a fit is appropriate. For these clumps, we compute $r_{\text{Gauss}} - r_{\text{core,corr}}$, finding that it does not correlate with $r_{\text{core,corr}}$; rather, it ranges between zero and 50 pc and has a median value of 25.5 pc. Assuming that this difference is a good representation of the value of $r_{\text{Gauss}} - r_{\text{core,corr}}$ for all of the $\text{H}\alpha$ -resolved clumps of our sample, we computed a new PSF-corrected core radius $\tilde{r}_{\text{core,corr}} = r_{\text{core,corr}} + 25.5$ pc. Therefore, the new sizes are $2\tilde{r}_{\text{core,corr}}$. The luminosities are recomputed by integrating the light within a circle of radius $3\tilde{r}_{\text{core,corr}}$. The procedure adopted in Wisnioski et al. (2012) to compute luminosity and size is similar to the one applied in Fisher et al. (2017), though not identical. Therefore, we are confident that

the corrections we applied to our clumps allow us to make a fair comparison with the results of Wisnioski et al. (2012).

Our clumps lie between the Fisher and Wisnioski relations, being closer to the one obtained by Fisher et al. (2017), even though they have lower luminosities and sizes compared to the peak of their distribution. With respect to the Wisnioski clump distribution, our resolved clumps are, on average, larger and, at a given size, brighter.

As shown by Johnson et al. (2017) and Cosens et al. (2018), DYNAMO clumps have both higher SFR and Σ_{SFR} than clumps in isolated spiral galaxies as a consequence of the starburst star formation of their hosting galaxies. Being closer to the DYNAMO sample in the luminosity–size relation may suggest that our H α -resolved clumps have a high Σ_{SFR} too (hints of that have already been found in Vulcani et al. 2020, in which they studied the resolved SFR–stellar mass relation for the MUSE H α clumps).

8. Catalog

We release the catalogs of H α - and UV-selected clumps separately as online tables. Each clump is univocally determined by the name of the galaxy, a letter (referring to the ASTRODENDRO run in which it was detected; see the Appendix), and an ID number. We then list the R.A. and decl. coordinates; the luminosity in the selection filter (not corrected for dust but corrected for N II in the case of H α -selected clumps); the morphological quantities (area, major and minor sigma, position angle, core radius, and PSF-corrected core radius); the photometric fluxes and their errors in each band, including F680N continuum-subtracted (H α + N II); a flag for the clump properties in the tree structure (0 for trunks that are not leaves, 1 for trunks that are also leaves, 2 for branches, and 4 for leaves that are not trunks); a flag for the spatial category (0 for tail, 1 for extraplanar, and 2 for disk); and a flag for the BPT classification (0 for no BPT diagram available, 1 for star-forming, 2 for composite, 3 for AGN, and 4 for LINER). Details about how these quantities are computed are given in Sections 4.1 and 4.2.

As an example, in the Appendix (Table A3), we report the first 10 rows of the H α -selected clump catalog. For clarity, for some values, not all of the significant digits are reported.

9. Summary

In this paper, we have built a sample of star-forming clumps and complexes in six jellyfish galaxies using a set of HST images in five photometric bands. Clumps were detected independently in UV (~ 2700 Å) and H α in order to probe star formation on different timescales (Kennicutt 1998), while the star-forming complexes were detected from optical emission (~ 6000 Å) to fully recover the stellar content formed from the stripped material in each clump region. Clumps were also divided into three spatial categories to separately study clumps formed within the disk (disk clumps), clumps that likely originated in extraplanar gas but still close to the disk (extraplanar clumps), and clumps formed in the stripped gas outside of the galactic disk and embedded in the ICM (tail clumps). Also, clumps in the tail give the unprecedented opportunity to study young stellar populations with no influence or underlying contamination by the stellar disk.

The method we use to detect clumps (Section 4.1) yields the hierarchical cascade structure of these star-forming regions.

While disk clumps are often characterized by complex structures where many clumps are localized in bigger structures, extraplanar and tail clumps are typically simple structures with no subregions. Moreover, tail clumps tend to be aligned in elongated or arched structures along RPS subtails. Interestingly, the H α -selected clumps, UV-selected clumps, and F606W star-forming complexes are often nested into each other, with H α -selected clumps being embedded in larger UV-selected clumps and star-forming complexes sometimes containing several UV- and H α -selected clumps.

The final samples comprise 2406 H α -selected clumps (1708 disk, 375 extraplanar, and 323 tail clumps), 3745 UV-selected clumps (2021 disk, 825 extraplanar, and 899 tail clumps), and 424 star-forming complexes (located only in the tails by construction). The covered luminosity range is from $\sim 3 \times 10^{38}$ to $\sim 4 \times 10^{40}$ erg s $^{-1}$ in H α and $\sim 3 \times 10^{36}$ to $\sim 2 \times 10^{39}$ erg s $^{-1}$ Å $^{-1}$ in UV. On average, $\sim 15\%$ of them are resolved, meaning that their sizes are larger than ~ 140 pc, up to more than 1 kpc.

We studied the LDFs, SDFs, and luminosity–size relations of H α - and UV-selected clumps as a function of the spatial category. The LDF slopes averaged on all of the spatial categories are 1.84 ± 0.03 for H α -selected clumps and 1.73 ± 0.09 for UV-selected clumps. The average slopes of the SDFs are 3.6 ± 0.6 for H α -resolved clumps and 3.1 ± 0.3 for UV-resolved clumps. Finally, the average slopes of the luminosity–size relations are 2.3 ± 0.4 for H α -resolved clumps and 1.97 ± 0.17 for UV-resolved clumps. We find no clear difference among disk, extraplanar, and tail clumps. The best-fitting slopes of these distributions and relations are consistent among each other, as well as with the results obtained in previous works (Kennicutt et al. 1989; Cook et al. 2016; Santoro et al. 2022) and with theoretical predictions of hierarchical turbulence-driven star formation (Elmegreen & Falgarone 1996; Elmegreen 2006). On the other hand, the luminosity–size relation of the H α -resolved clumps is more similar to that of clumps in starburst galaxies; therefore, it suggests that these clumps, regardless of the spatial category, are experiencing an enhancement in Σ_{SFR} . These preliminary results suggest that ram pressure compresses the ISM and increases the H α luminosity of the clumps, while neither the presence of a disk and its gravity nor the gaseous conditions of the surrounding medium have a strong impact on the star formation process once the cold gas cloud conditions are set.

Future works on the mass, age, and star formation of the clumps; trends and gradients with the distance from the galaxies; and their fate will elucidate how and how much these clumps differ from those in undisturbed galaxies in order to shed light on the effects of ram pressure on the galactic ISM and of environment on star formation.

We are grateful to the anonymous referee for their useful comments that helped improve this manuscript. E.G. would like to thank A. Ignesti, A. Wolter, A. Marasco, R. Smith, K. George, and the GASP team for the useful discussions and comments. We would also like to thank Emily Wisnioski for providing us the data from her paper. This paper is based on observations made with the NASA/ESA Hubble Space Telescope obtained from the Space Telescope Science Institute, which is operated by the Association of Universities for Research in Astronomy, Inc., under NASA contract NAS 5-26555. These observations are under the program GO-16223.

All of the HST data used in this paper can be found in MAST: doi:10.17909/tms2-9250. This paper also used observations collected at the European Organization for Astronomical Research in the Southern Hemisphere associated with ESO program 196.B-0578. This research made use of Astropy, a community-developed core Python package for astronomy by the Astropy Collaboration (Price-Whelan et al. 2018). This project has received funding from the European Research Council (ERC) under the European Union’s Horizon 2020 research and innovation program (grant agreement No. 833824) and “INAF main-streams” funding program (PI: B. Vulcani).

Appendix ASTRODENDRO Parameter Setting

Three parameters regulate how ASTRODENDRO builds the tree structure.

1. **MIN_VALUE.** The algorithm stops when the flux threshold reaches this value instead of zero.
2. **MIN_NPIX.** The minimum number of pixels for a clump to be included in the tree structure.
3. **MIN_DELTA.** The threshold is not lowered in a continuum way but at steps of MIN_DELTA. If no MIN_DELTA is given, the algorithm identifies each local maximum as a new subclump. MIN_DELTA should be high enough to avoid the detection of noise peaks in the surface brightness distribution as subclumps.

We performed three runs of ASTRODENDRO for the F275W and H α images of each galaxy, adopting the following parameters (MIN_NPIX = 5 in all runs). The number of clumps detected in each filter at each run are listed in Table A1.

1. Run A: MIN_VALUE = 2.5σ ; MIN_DELTA = 5σ .
2. Run B: MIN_VALUE = 2.5σ ; no MIN_DELTA. Given that a clump candidate is detected only if its brightest pixel is brighter than about MIN_VALUE+MIN_DELTA, regions for which each pixel has counts between MIN_VALUE and MIN_VALUE+MIN_DELTA are not detected. Since we want to also detect these fainter clumps, we run ASTRODENDRO a second time without defining MIN_DELTA. This run is executed on an image masked for the clumps detected in run A, and only trunk clumps are retained to avoid including spurious local maxima.
3. Run C: MIN_VALUE = 2σ ; no MIN_DELTA. This run is performed on an image masked for the clumps detected and kept in runs A and B. For the same reasons explained for run B, we kept only the trunk clumps of run C. Also, as a consequence of removing the high-frequency components of the image, denoising introduces a sort of smoothing, and part of the light of the brightest regions of the image, already detected as clumps, may eventually smooth out of the masks defined from runs A and B. Thus, even when masking the image for the clumps already detected, the residual smoothed emission adjacent to these masks may possibly be flagged as a clump in run C. Since such an emission is clearly not due to a real clump, we excluded from the sample generated by run C all clump candidates adjacent to the clumps found in the previous runs.

In the case of the F606W images, ASTRODENDRO was run on the denoised F606W images with MIN_VALUE = 3σ and no MIN_DELTA.

Table A1
Summary of the Number of Clumps in Each Subsample Used throughout This Paper, Depending on the Galaxy and Spatial Category

Filter (1)	Gal. (2)	LT Sample			Resolved Sample		
		A (3)	B (4)	C (5)	A (6)	B (7)	C (8)
H α	JO175	65(65)	214(214)	11(11)	31(31)	7(7)	0(0)
	JO201	206(165)	438(296)	19(15)	97(81)	18(7)	0(0)
	JO204	81(60)	287(233)	5(3)	36(29)	4(1)	0(0)
	JO206	99(84)	318(274)	21(19)	41(34)	3(3)	0(0)
	JW39	27(20)	198(143)	10(5)	11(9)	3(3)	0(0)
	JW100	94(40)	299(232)	14(12)	29(13)	6(5)	0(0)
	Total	572(434)	1754(1392)	80(65)	245(197)	41(26)	0(0)
UV	JO175	74(74)	204(204)	9(9)	35(35)	7(7)	0(0)
	JO201	399(372)	779(670)	66(58)	198(180)	35(31)	0(0)
	JO204	106(102)	397(348)	28(25)	68(65)	14(13)	0(0)
	JO206	137(135)	573(568)	31(30)	82(80)	24(24)	0(0)
	JW39	55(55)	282(276)	18(18)	28(8)	3(3)	0(0)
	JW100	173(152)	392(362)	22(19)	80(67)	12(11)	0(0)
	Total	949(891)	2627(2428)	174(159)	491(455)	100(94)	0(0)

Note. Number of clumps detected in each galaxy, depending on the ASTRODENDRO run. The columns are as follows: (1) the photometric band in which the clumps were detected; (2) the name of the galaxy; (3)–(5) the number of clumps in the LT sample detected in runs A, B, and C; and (6)–(8) the number of clumps in the resolved sample detected in runs A, B, and C. Parentheses enclose the number of clumps in the same sample but selected in order to avoid regions powered by AGN emission (see Section 4.2).

Table A2
K-S Test P Values

(1)	$H\alpha$			UV		
	D-E (2)	D-T (3)	E-T (4)	D-E (5)	D-T (6)	E-T (7)
Lum.	0.792	0.350	0.254	0.004	2×10^{-8}	0.152
Size	3×10^{-6}	0.613	0.012	7×10^{-5}	9×10^{-4}	0.002

Note. The P values of K-S tests (Section 6.1) for luminosity (first row) and size distributions (second row). Columns (2)–(4) list the values for the $H\alpha$ -selected clumps when comparing disk and extraplanar (D-E), disk and tail (D-T), and extraplanar and tail (E-T) clumps, respectively. Columns (5)–(7) show the same results but for UV-selected clumps. The $H\alpha$ -selected clumps are also selected to avoid AGN-powered regions when performing the K-S test on the luminosity distributions.

Table A3
(a) First 10 Rows of the Catalog of $H\alpha$ -selected Clumps Available Online. (b)–(d) First 10 Rows of the $H\alpha$ -selected Clump Catalog

(a)										
ID_clump	Galaxy	id_cat	_idx	R.A.	Decl.	Lum.	errL	A	σ_M	σ_m
(1)	(2)	(3)	(4)	deg (5)	deg (6)	erg s ⁻¹ (7)	erg s ⁻¹ (8)	arcsec ² (9)	arcsec (10)	arcsec (11)
JO175_A6_halfalpha	JO175	A	6	312.851	-52.834	3.264e+38	2.236e+37	0.040	0.071	0.041
JO175_A10_halfalpha	JO175	A	10	312.829	-52.827	6.320e+38	2.865e+37	0.061	0.091	0.046
JO175_A11_halfalpha	JO175	A	11	312.829	-52.827	1.979e+39	4.976e+37	0.173	0.137	0.080
JO175_A15_halfalpha	JO175	A	15	312.823	-52.824	1.068e+38	1.339e+37	0.016	0.060	0.026
JO175_A16_halfalpha	JO175	A	16	312.824	-52.823	3.202e+38	2.193e+37	0.038	0.055	0.047
JO175_A17_halfalpha	JO175	A	17	312.823	-52.823	8.186e+38	3.692e+37	0.106	0.111	0.088
JO175_A18_halfalpha	JO175	A	18	312.823	-52.823	2.851e+38	1.742e+37	0.022	0.050	0.025
JO175_A19_halfalpha	JO175	A	19	312.823	-52.823	3.118e+39	6.811e+37	0.336	0.267	0.123
JO175_A20_halfalpha	JO175	A	20	312.824	-52.823	1.183e+39	3.940e+37	0.112	0.094	0.080
JO175_A21_halfalpha	JO175	A	21	312.819	-52.823	2.433e+38	2.055e+37	0.035	0.059	0.055
(b)										
θ	r_{core}	$r_{\text{core,corr}}$	F275W		errF275W		F336W			
deg	arcsec	kpc	erg $\text{\AA}^{-1} \text{s}^{-1} \text{cm}^{-2}$		erg $\text{\AA}^{-1} \text{s}^{-1} \text{cm}^{-2}$		erg $\text{\AA}^{-1} \text{s}^{-1} \text{cm}^{-2}$			
(12)	(13)	(14)	(15)		(16)		(17)			
174.007	5.383e-02	4.027e-02	6.931e-19		4.989e-20		4.697e-19			
-155.162	6.429e-02	5.116e-02	1.321e-18		6.366e-20		8.863e-19			
-163.439	1.050e-01	9.040e-02	3.742e-18		1.092e-19		2.674e-18			
120.172	3.928e-02	2.300e-02	5.896e-20		2.790e-20		2.779e-20			
149.070	5.085e-02	3.701e-02	1.767e-19		4.521e-20		2.139e-19			
117.811	9.889e-02	8.468e-02	2.876e-18		8.714e-20		2.590e-18			
114.278	3.533e-02	1.706e-02	1.080e-19		3.385e-20		1.221e-19			
-149.026	1.810e-01	1.603e-01	5.979e-18		1.504e-19		5.986e-18			
118.371	8.677e-02	7.318e-02	2.055e-18		8.589e-20		2.233e-18			
106.350	5.689e-02	4.352e-02	1.504e-19		4.306e-20		1.526e-19			
(c)										
errF336W	F606W	errF606W	F680N		errF680N		F814W			
erg $\text{\AA}^{-1} \text{s}^{-1} \text{cm}^{-2}$	erg $\text{\AA}^{-1} \text{s}^{-1} \text{cm}^{-2}$	erg $\text{\AA}^{-1} \text{s}^{-1} \text{cm}^{-2}$	erg $\text{\AA}^{-1} \text{s}^{-1} \text{cm}^{-2}$		erg $\text{\AA}^{-1} \text{s}^{-1} \text{cm}^{-2}$		erg $\text{\AA}^{-1} \text{s}^{-1} \text{cm}^{-2}$			
(18)	(19)	(20)	(21)		(22)		(23)			
3.332e-20	1.636e-19	7.199e-21	3.663e-19		1.761e-20		6.024e-20			
4.264e-20	4.281e-19	1.003e-20	7.618e-19		2.318e-20		1.010e-19			
7.370e-20	1.191e-18	1.703e-20	2.308e-18		4.012e-20		3.208e-19			
1.809e-20	3.245e-20	3.987e-21	1.104e-19		1.035e-20		2.372e-20			
3.051e-20	3.086e-19	8.181e-21	5.045e-19		1.843e-20		2.006e-19			
6.171e-20	2.520e-18	1.948e-20	2.837e-18		3.703e-20		1.847e-18			
2.281e-20	3.534e-19	7.613e-21	5.500e-19		1.626e-20		3.052e-19			
1.056e-19	8.298e-18	3.536e-20	9.999e-18		6.858e-20		6.803e-18			
6.131e-20	2.869e-18	2.062e-20	3.449e-18		3.973e-20		2.161e-18			
2.871e-20	1.442e-19	6.735e-21	3.060e-19		1.633e-20		9.034e-20			



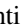


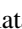

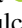
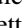
Table A3
(Continued.)

(d)					
errF814W	F680N_line_flux	errF680N_line_flux	dendro_flag	tail_gal_flag	BPT_flag
$\text{erg } \text{\AA}^{-1} \text{ s}^{-1} \text{ cm}^{-2}$	$\text{erg s}^{-1} \text{ cm}^{-2}$	$\text{erg s}^{-1} \text{ cm}^{-2}$			
(24)	(25)	(26)	(27)	(28)	(29)
8.368e−21	1.023e−16	7.008e−18	1	0	0
1.050e−20	1.981e−16	8.981e−18	1	0	0
1.820e−20	6.204e−16	1.560e−17	1	0	1
5.095e−21	3.347e−17	4.198e−18	1	2	1
9.345e−21	1.004e−16	6.875e−18	1	2	1
2.083e−20	2.566e−16	1.157e−17	1	2	1
8.726e−21	8.937e−17	5.459e−18	1	2	1
3.914e−20	9.773e−16	2.135e−17	1	2	1
2.211e−20	3.707e−16	1.235e−17	1	2	1
8.150e−21	7.624e−17	6.440e−18	1	0	1

Notes. (a) For clarity, for some values, not all of the significant digits are reported. Columns (1)–(11): ID of the clump (ID_clump), name of the host galaxy (galaxy), ASTRODENDRO run (id_cat; details in the Appendix), clump id (_idx), coordinates of the center (R.A. and decl.), luminosity and uncertainty in the selection filter (Lum. and errL; notice that H α luminosity is in erg s^{-1} and corrected to remove N II emission, while UV luminosity is in $\text{erg s}^{-1} \text{\AA}^{-1}$), area A, semimajor axis (major_sigma, σ_M), and semiminor axis (minor_sigma, σ_m). (b) Columns (12)–(17): position angle (θ), core radius (r_{core}), PSF-corrected core radius ($r_{\text{core,corr}}$), density flux and uncertainty in filter F275W (F275W and errF275W), and density flux in filter F336W (F336W). (c) Columns (18)–(23): uncertainty on the density flux in filter F336W (errF336W), density flux and uncertainty in filter F606W (F606W and errF606W), density flux and uncertainty in filter F680N (F680N and errF680N), and density flux in filter F814W (F814W). (d) Columns (24)–(29): uncertainty on filter F814W (errF814W), flux and uncertainty in continuum-subtracted F680N (F680N_line_flux and errF680N_line_flux; note that the units are $\text{erg s}^{-1} \text{ cm}^{-2}$ in this case), position of the clump in the tree hierarchy (dendro_flag), spatial category of the clump (tail_gal_flag), and BPT category (BPT_flag).

(This table is available in its entirety in machine-readable form.)

ORCID iDs

Eric Giunchi  <https://orcid.org/0000-0002-3818-1746>
 Marco Gullieuszik  <https://orcid.org/0000-0002-7296-9780>
 Bianca M. Poggianti  <https://orcid.org/0000-0001-8751-8360>
 Alessia Moretti  <https://orcid.org/0000-0002-1688-482X>
 Ariel Werle  <https://orcid.org/0000-0002-4382-8081>
 Claudia Scarlata  <https://orcid.org/0000-0002-9136-8876>
 Anita Zanella  <https://orcid.org/0000-0001-8600-7008>
 Benedetta Vulcani  <https://orcid.org/0000-0003-0980-1499>
 Daniela Calzetti  <https://orcid.org/0000-0002-5189-8004>

References

- Abramson, A., & Kenney, J. D. P. 2014, *AJ*, 147, 63
 Alstott, J., Bullmore, E., & Plenz, D. 2014, *PLoS*, 9, e85777
 Arsenault, R., & Roy, J. R. 1988, *A&A*, 201, 199
 Bacon, R., Accardo, M., Adjali, L., et al. 2010, *Proc. SPIE*, 7735, 773508
 Baldwin, J. A., Phillips, M. M., & Terlevich, R. 1981, *PASP*, 93, 5
 Bartolini, C., Ignesti, A., Gitti, M., et al. 2022, *ApJ*, 936, 74
 Bastian, N., Ercolano, B., Gieles, M., et al. 2007, *MNRAS*, 379, 1302
 Beckman, J. E., Rozas, M., Zurita, A., Watson, R. A., & Knapen, J. H. 2000, *AJ*, 119, 2728
 Bellhouse, C., Jaffé, Y. L., Hau, G. K. T., et al. 2017, *ApJ*, 844, 49
 Bellhouse, C., Jaffé, Y. L., McGee, S. L., et al. 2019, *MNRAS*, 485, 1157
 Bellhouse, C., McGee, S. L., Smith, R., et al. 2021, *MNRAS*, 500, 1285
 Biviano, A., Moretti, A., Paccagnella, A., et al. 2017, *A&A*, 607, A81
 Calzetti, D., Lee, J. C., Sabbi, E., et al. 2015, *AJ*, 149, 51
 Campitiello, M. G., Ignesti, A., Gitti, M., et al. 2021, *ApJ*, 911, 144
 Cardelli, J. A., Clayton, G. C., & Mathis, J. S. 1989, *ApJ*, 345, 245
 Cava, A., Bettoni, D., Poggianti, B. M., et al. 2009, *A&A*, 495, 707
 Chabrier, G. 2003, *PASP*, 115, 763
 Clauset, A., Shalizi, C. R., & Newman, M. E. J. 2009, *SIAMR*, 51, 661
 Consolandi, G., Gavazzi, G., Fossati, M., et al. 2017, *A&A*, 606, A83
 Cook, D. O., Dale, D. A., Lee, J. C., et al. 2016, *MNRAS*, 462, 3766
 Cortese, L., Catinella, B., & Smith, R. 2021, *PASA*, 38, e035
 Cosens, M., Wright, S. A., Mieda, E., et al. 2018, *ApJ*, 869, 11
 Cramer, W. J., Kenney, J. D. P., Sun, M., et al. 2019, *ApJ*, 870, 63
 Deb, T., Verheijen, M. A. W., Gullieuszik, M., et al. 2020, *MNRAS*, 494, 5029
 Dessauges-Zavadsky, M., & Adamo, A. 2018, *MNRAS*, 479, L118
 Elmegreen, B. G. 2006, *ApJ*, 648, 572
 Elmegreen, B. G., & Falgarone, E. 1996, *ApJ*, 471, 816
 Elmegreen, D. M., Elmegreen, B. G., Adamo, A., et al. 2014, *ApJL*, 787, L15
 Farrens, S., Grigis, A., El Gueddari, L., et al. 2020, *A&C*, 32, 100402
 Fisher, D. B., Glazebrook, K., Damjanov, I., et al. 2017, *MNRAS*, 464, 491
 Fossati, M., Fumagalli, M., Boselli, A., et al. 2016, *MNRAS*, 455, 2028
 Franchetto, A., Vulcani, B., Poggianti, B. M., et al. 2020, *ApJ*, 895, 106
 Fritz, J., Moretti, A., Gullieuszik, M., et al. 2017, *ApJ*, 848, 132
 Fujii, M. S., & Portegies Zwart, S. 2015, *MNRAS*, 449, 726
 Gallagher, J. S., & Hunter, D. A. 1983, *ApJ*, 274, 141
 George, K., Poggianti, B. M., Bellhouse, C., et al. 2019, *MNRAS*, 487, 3102
 George, K., Poggianti, B. M., Gullieuszik, M., et al. 2018, *MNRAS*, 479, 4126
 Gieles, M. 2009, *Ap&SS*, 324, 299
 Gouliermis, D. A., Elmegreen, B. G., Elmegreen, D. M., et al. 2017, *MNRAS*, 468, 509
 Gouliermis, D. A., Thilker, D., Elmegreen, B. G., et al. 2015, *MNRAS*, 452, 3508
 Grasha, K., Elmegreen, B. G., Calzetti, D., et al. 2017, *ApJ*, 842, 25
 Gullieuszik, M., Giunchi, E., Poggianti, B. M., et al. 2023, *ApJ*, 945, 54
 Gullieuszik, M., Poggianti, B. M., McGee, S. L., et al. 2020, *ApJ*, 899, 13
 Gullieuszik, M., Poggianti, B. M., Moretti, A., et al. 2017, *ApJ*, 846, 27
 Gunn, J. E., Gott, J., & Richard, I. 1972, *ApJ*, 176, 1
 Gusev, A. S. 2014, *MNRAS*, 442, 3711
 Haydon, D. T., Kruijssen, J. M. D., Chevance, M., et al. 2020, *MNRAS*, 498, 235
 Ignesti, A., Vulcani, B., Poggianti, B. M., et al. 2022a, *ApJ*, 924, 64
 Ignesti, A., Vulcani, B., Poggianti, B. M., et al. 2022b, *ApJ*, 937, 58
 Jáchym, P., Kenney, J. D. P., Sun, M., et al. 2019, *ApJ*, 883, 145
 Johnson, T. L., Rigby, J. R., Sharon, K., et al. 2017, *ApJL*, 843, L21
 Kauffmann, G., Heckman, T. M., Tremonti, C., et al. 2003, *MNRAS*, 346, 1055
 Kelly, B. C. 2007, *ApJ*, 665, 1489
 Kenney, J. D. P., Abramson, A., & Bravo-Alfaro, H. 2015, *AJ*, 150, 59
 Kennicutt, R. C., & Evans, N. J. 2012, *ARA&A*, 50, 531
 Kennicutt, R. C., & Hodge, P. W. 1980, *ApJ*, 241, 573
 Kennicutt, R. C. J. 1998, *ARA&A*, 36, 189
 Kennicutt, R. C. J., Armus, L., Bendo, G., et al. 2003, *PASP*, 115, 928
 Kennicutt, R. C. J., Edgar, B. K., & Hodge, P. W. 1989, *ApJ*, 337, 761
 Kewley, L. J., Heisler, C. A., Dopita, M. A., & Lumsden, S. 2001, *ApJS*, 132, 37
 Klaus, A., Yu, S., & Plenz, D. 2011, *PLoS*, 6, e19779

- Larsen, S. S. 2002, *AJ*, 124, 1393
- Lee, J. C., Thilker, D., Whitmore, B., et al. 2020, AAS Meeting, 235, 415.05
- Lee, J. H., Hwang, N., & Lee, M. G. 2011, *ApJ*, 735, 75
- Mascoop, J. L., Anderson, L. D., Wenger, T. V., et al. 2021, *ApJ*, 910, 159
- Merluzzi, P., Busarello, G., Dopita, M. A., et al. 2013, *MNRAS*, 429, 1747
- Messa, M., Adamo, A., Calzetti, D., et al. 2018, *MNRAS*, 477, 1683
- Messa, M., Adamo, A., Östlin, G., et al. 2019, *MNRAS*, 487, 4238
- Monreal-Ibero, A., Colina, L., Arribas, S., & García-Marín, M. 2007, *A&A*, 472, 421
- Moretti, A., Paladino, R., Poggianti, B. M., et al. 2018, *MNRAS*, 480, 2508
- Moretti, A., Paladino, R., Poggianti, B. M., et al. 2020, *ApJ*, 889, 9
- Nath, B. B., Das, P., & Oey, M. S. 2020, *MNRAS*, 493, 1034
- Peluso, G., Vulcani, B., Poggianti, B. M., et al. 2022, *ApJ*, 927, 130
- Poggianti, B. M., Fasano, G., Omizzolo, A., et al. 2016, *AJ*, 151, 78
- Poggianti, B. M., Gullieuszik, M., Tonnesen, S., et al. 2019, *MNRAS*, 482, 4466
- Poggianti, B. M., Ignesti, A., Gitti, M., et al. 2019, *ApJ*, 887, 155
- Poggianti, B. M., Moretti, A., Gullieuszik, M., et al. 2017a, *ApJ*, 844, 48
- Poggianti, B. M., Jaffé, Y. L., Moretti, A., et al. 2017b, *Natur*, 548, 304
- Portegies Zwart, S. F., McMillan, S. L. W., & Gieles, M. 2010, *ARA&A*, 48, 431
- Price-Whelan, A. M., Sipőcz, B. M., Günther, H. M., et al. 2018, *AJ*, 156, 123
- Radovich, M., Poggianti, B., Jaffé, Y. L., et al. 2019, *MNRAS*, 486, 486
- Ramatsoku, M., Serra, P., Poggianti, B. M., et al. 2020, *A&A*, 640, A22
- Rozas, M., Richer, M. G., López, J. A., Relaño, M., & Beckman, J. E. 2006, *A&A*, 455, 539
- Santoro, F., Kreckel, K., Belfiore, F., et al. 2022, *A&A*, 658, A188
- Schlafly, E. F., & Finkbeiner, D. P. 2011, *ApJ*, 737, 103
- Schlegel, D. J., Finkbeiner, D. P., & Davis, M. 1998, *ApJ*, 500, 525
- Sharp, R. G., & Bland-Hawthorn, J. 2010, *ApJ*, 711, 818
- Smith, R. J., Lucey, J. R., Hammer, D., et al. 2010, *MNRAS*, 408, 1417
- Sun, M., Ge, C., Luo, R., et al. 2021, *NatAs*, 6, 270
- Tomičić, N., Vulcani, B., Poggianti, B. M., et al. 2021a, *ApJ*, 907, 22
- Tomičić, N., Vulcani, B., Poggianti, B. M., et al. 2021b, *ApJ*, 922, 131
- Vulcani, B., Poggianti, B. M., Gullieuszik, M., et al. 2018, *ApJL*, 866, L25
- Vulcani, B., Poggianti, B. M., Tonnesen, S., et al. 2020, *ApJ*, 899, 98
- Whitmore, B. C., Chandar, R., Bowers, A. S., et al. 2014, *AJ*, 147, 78
- Wisnioski, E., Glazebrook, K., Blake, C., et al. 2012, *MNRAS*, 422, 3339
- Yoshida, M., Yagi, M., Komiyama, Y., et al. 2008, *ApJ*, 688, 918